Materials & Design 221 (2022) 110975

Contents lists available at ScienceDirect

Materials & Design

journal homepage: www.elsevier.com/locate/matdes

Tuning homogenization of high-strength aluminum alloys through thermodynamic alloying approach

Yawen Wang [a,f], Longgang Hou [a,d,e,*], Hui Su [a], Qingkun Tian [a], Kangcai Yu [a,g], Dmitry Eskin [d,h], Laurens Katgerman [i,j], Linzhong Zhuang [a,b,c,*]

[a] State Key Laboratory for Advanced Metals and Materials, University of Science and Technology Beijing, Beijing 100083, China
[b] Beijing Advanced Innovation Center for Materials Genome Engineering, University of Science and Technology Beijing, Beijing 100083, China
[c] Beijing Laboratory of Metallic Materials and Processing for Modern Transportation, University of Science and Technology Beijing, Beijing 100083, China
[d] BCAST, Brunel University London, Kingston Lane, Uxbridge Middlesex UB8 3PH, United Kingdom
[e] Nanjing Institute for Advanced Transportation Equipment and Technology, No. 8 Lanhua Road, Pukou District, Nanjing 211800, China
[f] CRRC Beijing Locomotive Co., Ltd., Beijing 100072, China
[g] Chinalco Materials Application Research Institution Co., Ltd., Beijing 102209, China
[h] Tomsk State University, Tomsk 634050, Russian Federation
[i] Katgerman Aluminium Technology, van Beuningenlaan 10, 2334CC Leiden, the Netherlands
[j] Department of Materials Science and Engineering, Delft University of Technology, Mekelweg 2, 2628CD Delft, the Netherlands

HIGHLIGHTS

- The relationship among the composition, microstructure and homogenization process for Al-Zn-Mg-Cu alloys was clarified by the experiments and thermodynamic calculations.
- The optimal one-/two-step homogenization processes were suggested based on the coarse residual phase.
- A critical (Cu + Mg) level (depending on the solubility limit) and a linear correlation between Cu and Mg contents (depending on the stoichiometric balance) were revealed for guiding the homogenization processes.
- A thermodynamic approach was established for composition design of Al-Zn-Mg-Cu alloys.

GRAPHICAL ABSTRACT

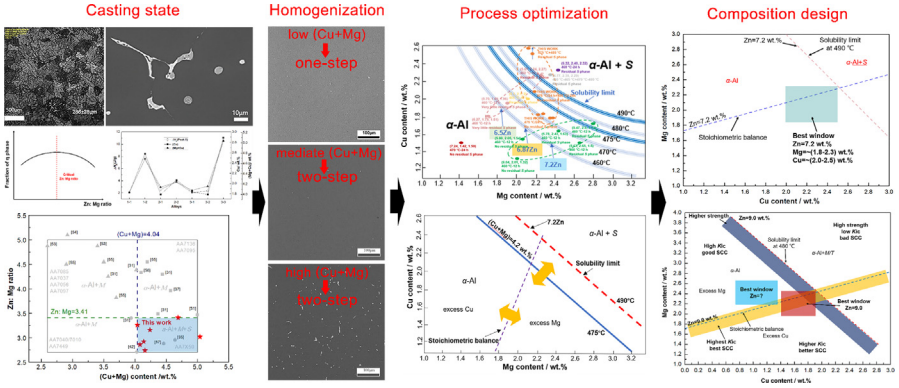

ARTICLE INFO

Article history:
Received 30 May 2022
Revised 13 July 2022
Accepted 20 July 2022
Available online 25 July 2022

Keywords:

ABSTRACT

The alloy design and homogenization processes are intimately associated with the microstructure, phase composition and performance for Al-Zn-Mg-Cu alloys. The microstructures and phase composition of a series of Al-Zn-Mg-Cu alloys before and after the homogenization treatments were investigated along with thermodynamic calculation to understand the underlying relationship. The eutectic microstructures (α-Al + *M* ($Mg(ZnAlCu)_2$)) are dominating with Cu-enriched [AlCuMgZn] particles, both depending on the Zn:Mg ratio and (Cu + Mg) content, in addition to minor constituent θ (Al_2Cu) and Al_7Cu_2Fe phases in the

* Corresponding authors at: State Key Laboratory for Advanced Metals and Materials, University of Science and Technology Beijing, Beijing 100083, China.
E-mail addresses: longgang.hou2@brunel.ac.uk (L. Hou), linzhongzhuang@163.com (L. Zhuang).

https://doi.org/10.1016/j.matdes.2022.110975

Aluminum alloys
Composition
Microstructure
Thermodynamic calculation
Homogenization

as-cast alloys. The optimal homogenization process was suggested based on the analysis of the residual phases (i.e., the *S* (Al_2CuMg) phase) since all (for low/mediate-(Cu + Mg) alloys) or partially (for high-(Cu + Mg) alloys (~>4.24 wt%)) *S* (Al_2CuMg) particles were dissolved during the homogenization. This residual *S* phase may be transformed from the primary *M* and/or Cu-enriched [AlCuMgZn] phases. The homogenization kinetics calculation results agreed well with above experimental results. A critical (Cu + Mg) level and a linear correlation between Cu and Mg concentrations were revealed based on the thermodynamically modelling, which can be conductive to determine the optimal homogenization process. Furthermore, the solubility limit and stoichiometric balance principles based on controlling the homogenized microstructures can guide the composition design for advanced high-strength aluminum alloys.

1. Introduction

The high-strength aluminum alloys, e.g. AA7075, AA7050, AA7055, AA7085, are commonly applied in the transportation industry [1-3] with long-term objective of better integrated properties such as high strength and fracture toughness, good corrosion resistance and high fatigue resistance [4-15]. These properties are highly impacted by the strengthening precipitates, dispersoids and coarse constituents, i. e., insoluble Cu-/Fe-rich intermetallics and the partially soluble *S* (Al_2CuMg) phase [7-9], as well as serious macro-/micro-segregation [12-16], all of which highly depend on the composition and processing [17-30]. Specifically, the soluble η ($MgZn_2$) phase or its precursors such as metastable η' and GP zones are mainly responsible for the alloy strength [7], while the workability and fracture behavior are highly affected by the soluble *T* ($Al_2Mg_3Zn_3$ or $Al_6Mg_{11}Zn_{11}$) phase, partially soluble *S* phase, insoluble Al_7Cu_2Fe and Mg_2Si phases [8,14,31-34], besides processing parameters. Additionally, the macro/micro-segregation may bring difficulty to the subsequent thermal-mechanical processing and deteriorate the final properties [13,16]. Thus, it is desirable to inhibit the formation of the *T* and *S* phases and control the contents and morphologies of the Al_7Cu_2Fe and Mg_2Si phases[8] during the solidification, while dissolving/eliminating the coarse intermetallic particles and segregation as much as possible by high-temperature treatments.

Most previous studies have been focused on the as-cast microstructures and phase composition for Al-Zn-Mg-Cu alloys, and it is generally believed that the as-cast alloys contain different combinations of the η, *T*, *S* and θ phases, i.e., η, *S* and θ phases in AA7050[35], η, *T*, *S* and θ phases in AA7055[19], η and θ phases in AA7085 alloys[36]. This indicates that the alloying strategies (such as adjusting the Zn:Mg ratio, the Cu:Mg ratio and/or (Mg + Cu) content) can play a substantial role in controlling the formation of these phases and are directly associated with final microstructures and properties. It is generally believed that the formation of the η phase is mainly affected by the Zn:Mg ratio, especially between 2.5 and 7.0[37], which is above the threshold Zn:Mg = 2.2 when the η phase begins to form [38]. In addition, thermodynamic calculation shows that the fraction of the *M* phase increases with Zn content in the low-Zn alloys (5.1–6.7 wt% Zn) but decreases with Mg content, which means that the high Zn:Mg ratios can promote the precipitation of the *M* phase [39]. However, the effect of Mg content on the precipitation of the η phase for high-Zn alloys (8.8–9.6 wt% Zn) is different from that of low-Zn alloys, i.e., with the increase of Mg content the fraction of the η phase firstly increases and then decreases, thus the effect of Zn and Mg contents on the fraction of the η phase needs more studies [40]. Furthermore, the non-equilibrium calculations show that the Mg content (2.0 and 2.5 wt%) in high-Zn alloys (9.2 and 9.8 wt%) has a greater effect on the fraction of the η phase than that of the Zn content [41], which is obviously different from the equilibrium calculation [39]. Therefore, the effect of Zn and/or Mg content on the formation and fraction of the η phase in the as-cast Al-Zn-Mg-Cu alloy can be well understood with a quantitative composition index, which would be vital for controlling the formation of the η phase.

It was considered that the solidified microstructures could contain the nonequilibrium *S* phase, in which the Cu sublattice were replaced partially by Zn atoms [19], but others believed that an unstable (Cu, Mg)- and/or Cu-enriched phase rather than the stable *S* phase might appear in the as-cast alloys [42]. Although the formation of the *S* or (Cu, Mg)- and/or Cu-enriched phase are correlated with the (Cu + Mg) content [19,43], there is still lack of effective approach to determine their formation in the as-cast state. It was shown that the high Cu and low Mg concentrations were favorable for the formation of the θ phase while the high Mg and low Cu concentrations for *T* phase [38], but there is no quantitative criterion for determining the formation of both phases. In addition, high-Zn Al-Zn-Mg-Cu alloys [~8.5 wt% Zn-(1.4 ~ 2.5) wt% Mg-(1.4 ~ 3.0) wt% Cu] only contain the η phase without the *T* and/or *S* phase [43], and the formation of the η phase can be promoted by high Mg and Cu concentrations, and the *S* or (Cu, Mg)- and/or Cu-enriched phase may appear in the as-cast alloys [19,43]. Definitely, the composition variation (i.e., Zn:Mg ratio and (Mg + Cu) content) can affect the complex precipitation and phase transformation by influencing the solidification thermodynamic parameters (such as the solidus and solvus lines of different phases) [44]. The systematic investigation about the comprehensive effects of the Zn/Mg/Cu composition could help in understanding the formation of the as-cast microstructures of the high-strength Al alloys.

The homogenization process as a critical manufacture step is applied for the ingots to dissolve and/or eliminate the low-melting point eutectic microstructures and secondary/constituent phases formed during solidification so as to benefit the workability, hardening and final properties [45-51]. It is known that the η phase can be dissolved quickly while the dissolution of *T* and *S* phases is sluggish [19], and the remaining secondary/constituent phases may deteriorate the alloy properties under some homogenization treatments (i.e., <470 °C). Although high-temperature and/or long-time one-step homogenization treatments can decrease or eliminate some of the coarse constituent particles, the two-step or multi-step homogenization processes are also applied with considering the costs, efficiency and the risk of overburn at high temperatures [45,47,48]. These homogenization processes are mainly controlled by the diffusion of the Zn/Mg/Cu atoms, and the different responses of the constituent particles to the homogenization treatments depend on their chemistry. The effects of the Zn:Mg ratio and (Cu + Mg) content on the microstructure evolution during homogenization were explored for low-Zn Al-Zn-Mg-Cu alloys [13,14], which indicated that the *T* and *S* phases could be effectively controlled by adjusting both two

parameters, i.e., with the increase of the Zn: Mg ratio and the decrease of the (Cu + Mg) content, the *T* and *S* phases can be inhibited. However, the initial coarse (Cu, Mg)- and/or Cu-enriched phase or the *S* phase transformed during the homogenization cannot be completely eliminated even by a high-temperature and/or long-time treatment for some alloys such as having high (Cu + Mg) content and/or low Zn: Mg ratio [13,35,46]. Although high alloying levels can contribute to a higher strength [48], i.e., AA7136 alloy, it will complicate the as-cast microstructures and their evolution, i.e., coarse second phase or constituent particles and macro-/micro-segregation, both of those cannot be completely eliminated during subsequent heat treatments such as homogenization or solution treatment [48]. In addition, the alloy design was previously based on the equilibrium and/or non-equilibrium thermodynamic calculations and limited experiments, and the large differences/deviations between them (i.e., solidification path and phase components) may lead to a time-consuming and high-cost alloy development. Thus, the correlation between the microstructures, alloy compositions and homogenization processes still needs in-depth understanding aiming at the effectively guided alloy design.

In this study, a series of Al-Zn-Mg-Cu alloys with different Zn: Mg ratios and (Cu + Mg) contents were designed to study the microstructures and phase components before and after homogenization with thermodynamic calculation. The optimal homogenization process was suggested by understanding the relationship between the composition, microstructure and phase composition before and after the homogenization, and the principles based on the control of homogenization microstructures were proposed to guide the composition design of high-strength Al-Zn-Mg-Cu alloys. This may pave a way for a reliable and accurate composition regulation for Al and other alloys.

2. Experimental procedure

A series of Al-Zn-Mg-Cu alloys (with the compositions in Table 1 measured by the Inductively Coupled Plasma-Atomic Emission Spectrometry (ICP-AES, GB/T 20975.25-2008)) were prepared with high purity Al (99.99 %), Zn (99.99 %), Mg (99.99 %), and Al-50 Cu, Al-10 Zr, Al-10 Ti and Al-5 Ti-B (wt%) master alloys. The raw materials were melted in an electric resistance furnace at 730–780 °C and then poured into a water-cooled steel mold at 690–725 °C with average 2 ∼ 3 °C /s cooling rate for ingots with sizes of 210 mm × 120 mm × 100 mm. Specimens with dimensions of 12 mm × 12 mm × 12 mm were cut from the quarter thickness position of these ingots.

Some of these samples were heated to 475 ± 2 °C (heating rate: 30 °C/h) and held for 18/24 h in an air furnace with subsequently quenching into room-temperature water. A two-step homogenization process (475 °C/24 h + 485 °C/12 or 24 h) was also applied. Other samples were additionally treated at 465/470 °C for 24 h. A 3 mm-diameter disc (∼10 mg) was tested in a TA2910 differential scanning calorimeter (DSC, heating rate: 10 °C/min) to measure the transformation temperatures with high purity aluminum disc of the same weight as a reference.

Metallographic samples were mechanically polished and etched with a solution of 2.5 vol% HNO_3 + 1.5 vol% HCl + 1 vol% HF, and observed using a Zeiss Axiovert 200 MAT model optical microscope (OM). The mechanically polished samples were analyzed by a scanning electron microscope (SEM) (ZEISS LEO 1450) equipped with an energy dispersive X-ray spectroscopy (EDS, Kevex SIGMA). The area fraction of the micron-sized particles in the as-cast and homogenized samples were measured and averaged from at least three SEM images (magnification: × 200) using the Image-Pro Plus image analysis software. It is known that the quantitative EDS results may be affected by the matrix composition under different acceleration voltages, which in turn may affect the electron beam penetration depth. After several trials, we used an acceleration voltage of 10 kV for EDS analysis combined with the multiple point or micro-zone analysis with similar features in order to decrease the electron beam deflection-induced error for a reliable composition information. X-ray diffraction (XRD) analysis was performed in a Rigaku DMAX-RB X-ray diffractometer (Cu Kα-Al radiation; working voltage: 40 kV; step length: 0.02°; scanning rate: 9°/min, Rigaku Corporation, Tokyo, Japan). Thermo-Calc thermodynamic software (TCS Al-based Alloy Database-TCAL8) was used to calculate phase diagrams and equilibrium/non-equilibrium (Schiel simulation) solidification process. If the solidification is very slow, and the alloy system is always maintained in the thermodynamic equilibrium state, and solutes in solid and liquid phases can be fully diffused for the equilibrium calculation. The Schiel simulation assumes that if the solidification is faster, the solute atoms cannot be diffused in the solid but still can fully diffuse in the liquid phase [43]. The real process may fall in between both conditions.

3. Results

3.1. Microstructure and phase constituents of the as-cast alloys

Typical aluminum dendrites and eutectic structures appear in the as-cast alloys (Fig. 1(a-c)) and the grain size seems to be gradually refined with higher solute levels, as reported previously [19,43]. The metallographic statistics show that the average dendrite arm spacing L [52] in the alloys 1-2, 2-2 and 3-3 are 45 μm, 39 μm and 47 μm, respectively, while 23-26 μm in the alloys 1-1, 2-1, 3-1 and 3-2. The significant interdendritic solute segregation [52] occurs for the alloys with the higher solute level or (Cu + Mg) content. Fig. 1(d-j) shows the white reticulated phase mainly along grain boundaries or in the interdendritic regions in the alloys 1-2, 3-1 and 3-3, while a few gray phase particles near the white phase only appear in the alloys 1-1, 1-2, 2-2, 3-1 and 3-3. Table S1 shows that the white phase with wide composition range can be identified as the non-equilibrium *M* phase with the crystal structure similar to the η phase [45]. In addition, some white particles with Cu content different from that of the *M* or *S* phase appear, namely a Cu-enriched phase (or [AlCuMgZn]

Table 1
Chemical compositions of the present alloys (wt%).

Alloys	Zn	Mg	Cu	Zr	Zn + Mg + Cu	Zn + Mg	Zn/Mg	Cu/Mg	Cu + Mg
1-1	7.20	2.21	1.83	0.090	11.24	9.41	3.26	0.83	4.04
1-2	7.20	2.11	2.58	0.098	11.89	9.31	3.41	1.22	4.69
2-1	6.87	2.35	1.79	0.10	11.01	9.22	2.92	0.76	4.14
2-2	6.86	2.17	2.07	0.10	11.10	9.03	3.16	0.95	4.24
3-1	6.40	2.24	1.84	0.10	10.48	8.64	2.86	0.82	4.08
3-2	6.50	2.37	1.79	0.10	10.66	8.87	2.74	0.76	4.16
3-3	6.50	2.15	2.89	0.10	11.54	8.65	3.02	1.34	5.04

Fe,Si < 0.08, Ti, Mn, Cr < 0.05, Al balance

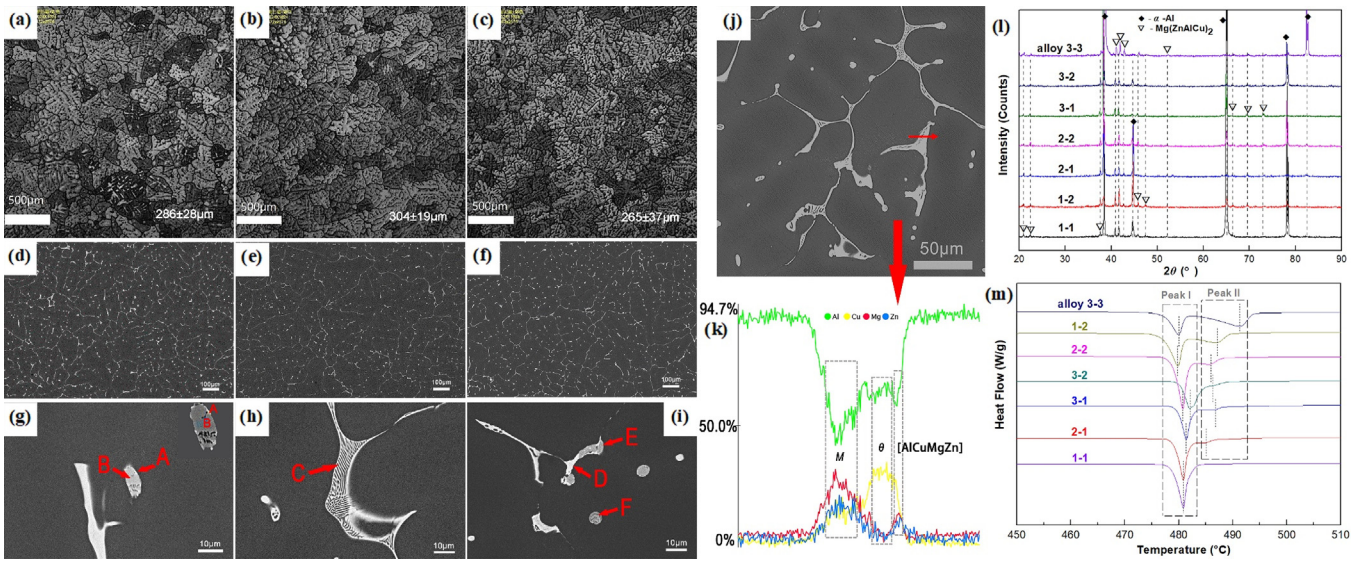

Fig. 1. Optical microstructures (a-c), SEM images (d-j), XRD patterns (l) and DSC curves (m) of the as-cast alloys: (a) 1-1; (b) 2-2; (c, f, i) 3-3; (d, g) 1-2; (e, h) 3-1; (j, k) line scan analysis.

phase)[42]. The non-equilibrium *M* phase exists in all alloys but the [AlCuMgZn] phase only appears in some alloys, i.e., 1-2, 2-1, 2-2, 3-1, 3-2 and 3-3 (Table S1). Fig. 1(j, k) and Table S1 show that the Al:Cu ratio in the gray phase adjacent to the [AlCuMgZn] phase is close to 2:1, which is identified as θ phase [7] in the alloys 1-1, 1-2, 3-1 and 3-3. Besides, the [AlCuMgZn] phase (as-arrowed by F in Fig. 1(i)) also appears as a divorced phase in the interdendritic regions. XRD results (Fig. 1(l)) are consistent with SEM observation. No θ phase appears in Fig. 1(l) because of its small concentration, and the [AlCuMgZn] phase may be isomorphous to the *M* or *S* phase[42,53], which needs more analysis.

Fig. 1(m) shows the DSC curves of the as-cast alloys and the peak temperature T_P and reaction heat ΔH_R associated with phase transformation are calculated and listed in Table 2. There are one (peak I) or two (peak I and II) endothermic peaks in each DSC curve: peak I: 479.8–482.0 °C, corresponding to the dissolution of eutectic microstructures (α-Al + *M*) [45,54,55]; Peak II: 484.4–49 1.3 °C, corresponding to the dissolution of the *S* phase [56,57] or Cu-enriched phase [42], which is likely overlapped with peak I. The endothermic peaks relating to θ and Al_7Cu_2Fe phases do not appear in the as-cast alloys due to their small fractions and/or high melting temperatures. It can be seen that the alloy 1-1 mainly contains the *M* phase, and the alloys 2-1, 3-1 and 3-2 additionally contain some *S* or [AlCuMgZn] phase, while the alloys 1-2, 2-2 and 3-3 mainly contain the *M* and *S* or [AlCuMgZn] phases, which is consistent with SEM observations above. Table 2 also shows that the reaction heat ΔH_R is proportional to the statistic volume fraction of the phase dissolved, which is in line with previous reports [58].

3.2. Microstructures and phase constituents after one-step homogenization

Only a few *M* and/or [AlCuZnMg] (i.e., Cu-enriched phase as will be discussed in 4.1) phase particles remain in all alloys and the insoluble Al_7Cu_2Fe phase is present in some alloys, i.e., the alloys 1-1, 1-2, 2-1 and 2-2 (Fig. 2 and Table S2) after the initial homogenization treatment at 475 °C for 24 h based on the DSC results in Fig. 1(m). Finally, only a few residual *M* and/or [AlCuZnMg] and *S* phase particles appear in the alloys 1-1, 2-1, 3-1 and 3-2, and more *S* phase appears in the alloys 1-2, 2-2 and 3-3, along with a few adjacent *M* and/or [AlCuZnMg] particles. The statistical area fraction of the second phases in Table S2 shows an obvious reduction after one-step homogenization but it remains still high in the alloys 1-2, 2-2 and 3-3 because of the residual *S* phase.

The homogenization treatment was also performed at 465 °C and 470 °C to compare the phase dissolution and transformation at different temperatures. A large number of gray *S* and white *M* phases are detected after the homogenization of the alloys 1-1, 2-1, 3-1 and 3-2 at 465 °C for 24 h (Fig. 3(a, d, g, j)), and the total area fractions of the second phases in these four alloys are 1.550 ± 0.010 %, 1.190 ± 0.005 %, 1.400 ± 0.007 % and 1.500 ± 0.007 %, respectively. The statistic results based on the contrast difference of different phases indicate that the area fractions of the white *M* phase are 0.410 ± 0.005%, 0.080 ± 0.003%, 0.090 ± 0.001% and 0.0 50 ± 0.001%, and the area fraction of the gray *S* phase are 0.850 ± 0.006%, 1.060 ± 0.004%, 1.320 ± 0.006% and 1.390 ± 0.005% in these four alloys, respectively. The dominant *M* phase in the as-cast alloys disappears largely after 465 °C − 24 h homogenization, indi-

Table 2
Peak temperature T_P and reaction heat ΔH_R calculated from the DSC curves (in Fig. 1(m)) of the as-cast alloys.

Alloys	Peak I		Peak II		Peak I + II	Area fraction of second phase /%
	T_P(°C)	ΔH_R(J/g)	T_P(°C)	ΔH_R(J/g)	ΔH_R(J/g)	
1-1	480.9	11.254	–	–	11.254	3.36 ± 0.01
1-2	479.8	10.657	487.2	7.541	18.198	4.07 ± 0.01
2-1	480.9	10.086	484.4	2.551	12.637	3.58 ± 0.01
2-2	480.8	13.050	485.8	3.849	16.899	3.86 ± 0.01
3-1	481.4	8.232	486.7	2.053	10.285	3.21 ± 0.01
3-2	482.0	9.630	485.5	2.331	11.961	3.45 ± 0.01
3-3	480.0	8.267	491.3	10.551	18.819	4.36 ± 0.01

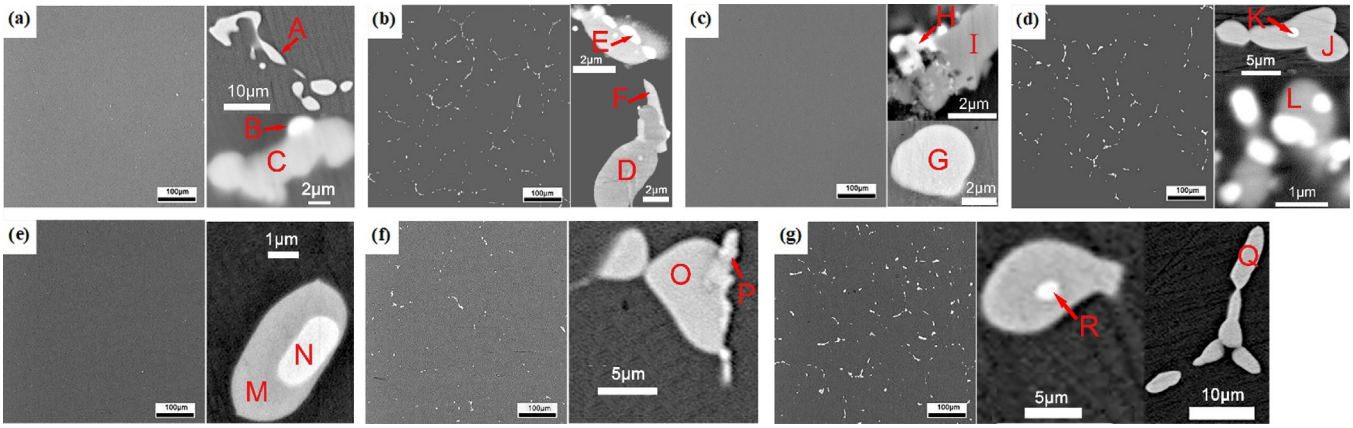

Fig. 2. SEM images of the one-step homogenized (475 °C/24 h) alloys: (a) 1-1, (b) 1-2, (c) 2-1, (d) 2-2, (e) 3-1, (f) 3-2, (g) 3-3.

cating that the second phases are dissolved and/or transformed to a large extent. The results show that the *S* phase is dominant along with the *M* phase, and no [AlCuZnMg] phase is found in the alloys 1-1, 2-1, 3-1 and 3-2. After the homogenization at 470 °C for 24 h, most of the second phases in the as-cast alloys disappear, and a few appear, i.e., the *S* phase, however most of the newly formed *S* phase transformed from the *M* phase and/or [AlCuZnMg] phase is dissolved during the homogenization (Fig. 3 (b, e, h, k)) [42,54,59]. In addition, there is still a few undissolved *M* particles (Fig. 3 (e, k)) and the insoluble Al_7Cu_2Fe phase (Fig. 3 (b, h)) adjacent to the newly formed *S* phase.

In addition, the calculated phase diagrams in Fig. 3(c, f, i, l) show that the alloys 1-1, 2-1, 3-1 and 3-2 are located in the [α-Al + *S*], [α-Al + *S*], [α-Al + *M* + *S*] and [α-Al + *M* + *S*] phase fields at 465 °C, respectively. It means that a longer time (≫24 h) is required for the homogenization of these four alloys at 465 °C while 470 °C is near the solvus of *S* phase (Fig. 3(c, f, i, l) and 11), and a short-time homogenization (i.e., =< 24 h) can completely dissolve the *M* and *S* phases [60].

The endothermic peaks I, II and III in Fig. 4 correspond to the dissolution of the *M* phase, [AlCuMgZn] phase and *S* phase, respectively. The weak endothermic peak I and the disappearance of the endothermic peak II in the alloys 1-1, 2-1 and 3-2 reveal that most of the *M* phase and all the [AlCuMgZn] phase are dissolved. However, the strong endothermic peak III in the alloys 2-1, 3-1 and 3-2 indicates that new *S* phase is formed although it may be partially dissolved [42,54,59,61]. Fig. 3 (a, d, g, j) shows that the *S* phase exists in the alloy 1-1 but with the lowest area fraction (∼0.85%) compared to others after homogenization at 465 °C for 24 h. Therefore, the endothermic peak III reflecting the *S* phase may not occur during the DSC test. However, no endothermic peak appears for the alloys 1-1 and 2-1 after homogenization at 470 °C and/or 475 °C for 24 h, which means that most of the *M* phase, all of the [AlCuMgZn] phase and the *S* phase transformed from the *M* phase [42,54,61] are dissolved. The weak endothermic peak III reveals that most of the *M* phase and all of the [AlCuMgZn] phase are dissolved besides a small amount of the *S* phase that is transformed from the *M* phase for the alloys 3-1 and 3-2 after homogenization at 470 °C for 24 h [42,54,59,61]. And there is no endothermic peak after homogenization at 475 °C for 24 h, indicating the complete dissolution. The above DSC analysis about the alloys 1-1, 2-1, 3-1 and 3-2 is basically consistent with SEM results except for a few remaining phases that could not be detected by the DSC test.

Furthermore, the alloys 1-1, 2-1, 3-1 and 3-2 homogenized at 475 °C for 18 h exhibit more residual *S* phase compared with that after 475 °C /24 h treatment (Fig.S2 and Table S4). In a word, the homogenization with 475 °C/24 h could be suitable for these ingots.

3.3. Microstructures and phase constituents after two-step homogenization

There are still a large number of second phases along grain boundaries (Fig. 5(a, d, g)), as well as a few spherical *S* particles (Table S3) in the alloys 1-2, 2-2 and 3-3 even after homogenizing at 475 °C for 24 h. The volume fraction of the *S* phase is further decreased except for a few spherical or short-rod *S* particles along grain boundaries after the two-step homogenization (475 °C/24 h + 485 °C/12 h) (Fig. 5(b, e, h)). The intragranular/intergranular distribution of the *S* phase in the alloys 1-2 and 3-3 does not change apparently but the *S* phase is almost dissolved in the alloy 2-2 with prolonging the second-step homogenization time to 24 h, as indicated in Fig. 5 (c, f, i), Table S5 and Table S3.

The peak temperature T_P and reaction heat ΔH_R from the DSC curves (Fig. 6) of the homogenized (one- and two-step) alloys as shown in Table S6 indicate that only the endothermic peak III (∼495 °C) after the two-step homogenization (475 °C/24 h + 485 °C/12 h or 475 °C/24 h + 485 °C/24 h) appears in the alloys 1-2, 2-2 and 3-3. And the peak intensity for the alloy 1-2 continuously decreases, corresponding to a continuous reduction of ΔH_R value, while the endothermic peaks of the alloys 2-2 and 1-3 after the homogenization with 475 °C/24 h + 485 °C/12 h are not noticeably weakened as compared with that after 475 °C/24 h treatment, which means no significant variation in the ΔH_R value. The endothermic peak completely disappears in the alloy 2-2 but not in the alloys 1-2 and 3-3 after the homogenization with 475 °C/24 h + 485 °C/24 h (Fig. 6). The DSC analysis of the alloys 1-2, 2-2 and 3-3 is consistent with the above SEM observations.

4. Discussion

4.1. Correlation between the alloy composition and solidification phases

The thermodynamic calculation shows that the equilibrium microstructures at room temperature are composed of four main phases: α-Al, *M*, $T_{(equilibrium)}$[$(AlCuZn)_{49}Mg_{32}$] and θ, being consistent with above as-cast microstructure results except for the $T_{(equilibrium)}$ phase below 80 °C (Fig. 7(a, b) and Table 3). This indicates that the $T_{(equilibrium)}$ phase has no correlation with the *S* phase or Cu-enriched phase, both of which can be dissolved at ∼490 °C (Fig. 1(m)) and do not exist at room temperature in Fig. 7(a, b) and Table 3. The solidification paths based on the Scheil model of

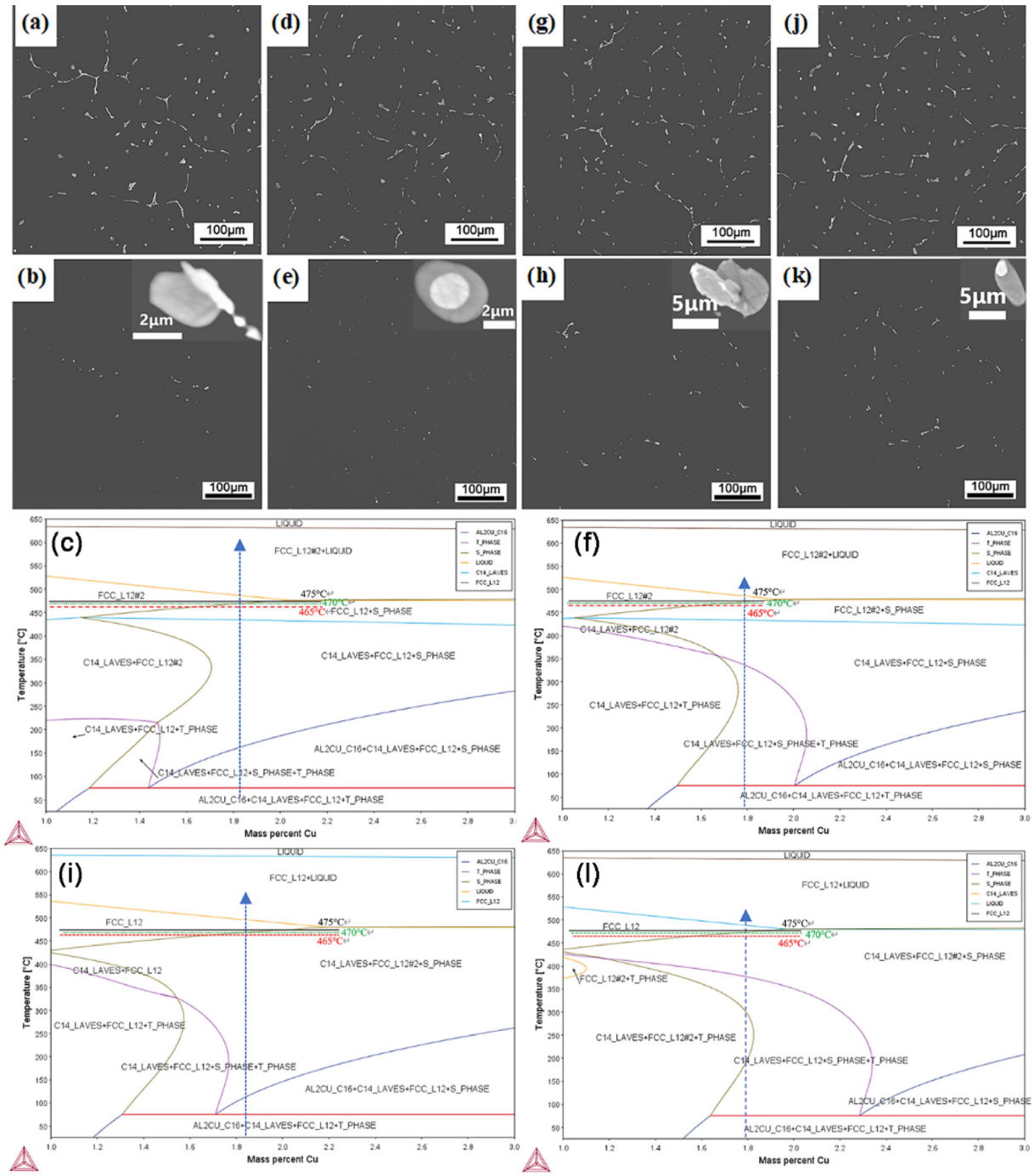

Fig. 3. SEM images of the one-step homogenized alloys with 465 °C/24 h (a, d, g, j) and 470 °C/24 h (b, e, h, k): (a, b) 1-1, (d, e) 2-1, (g, h) 3-1, (j, k) 3-2, and calculated isopleth of Al-Zn-Mg-xCu system with (c) 1-1: 7.20 wt% Zn and 2.21 wt% Mg; (f) 2-1: 6.87 wt% Zn and 2.35 wt% Mg; (i) 3-1: 6.40 wt% Zn and 2.24 wt% Mg; (l) 3-2: 6.50 wt% Zn and 2.37 wt% Mg.

the typical alloys in Fig. 7(c, d) indicate that the α-Al, $T_{(non\text{-}equilibrium)}$, *S* and *V* phases are formed successively during the solidification in the alloys 1-1 and 3-1 (low (Cu + Mg) content) while the α-Al, *S*, *V* and $T_{(non\text{-}equilibrium)}$ phases successively in the alloys 1-2 and 3-3 (high (Cu + Mg) content). Their final phase compositions are obviously inconsistent with the experimental results (Table S1). The *S* phase precipitates at ~462-472 °C during the solidification in these four alloys and then transforms (via transitional reactions) into the $T_{(non\text{-}equilibrium)}$ or *V* phase without the residual *S* phase (Fig. 7(d)), which is consistent with that of Fig. 1 (l, m) and Table S1. Thus, it can be considered that the *S* phase may transform into the *V* or $T_{(non\text{-}equilibrium)}$ phase during the solidification.

Some earlier studies showed mainly $MgZn_2$ and $Al_2Mg_3Zn_3$ phases or their isomorphous phases in the as-cast state without the *S* phase [36,49 54,61], and Cu sublattices in the *S* structure partially replaced by Zn atoms, thus forming the stoichiometric $Al_2Cu_XMgZn_{1-X}$ phase ((50–58)Al-(14–17)Zn-(19–23)Mg-(9–13)Cu, at.%)[19]. In addition, some Zn sublattices in the $MgZn_2$ structure can be replaced by Al and Cu atoms, thus forming the *M* phase (eventually forming AlCuMg phase), which also occurs in the $Al_2Mg_3Zn_3$ structure to form $Mg_3(AlCuZn)_2$ phase (eventually in the

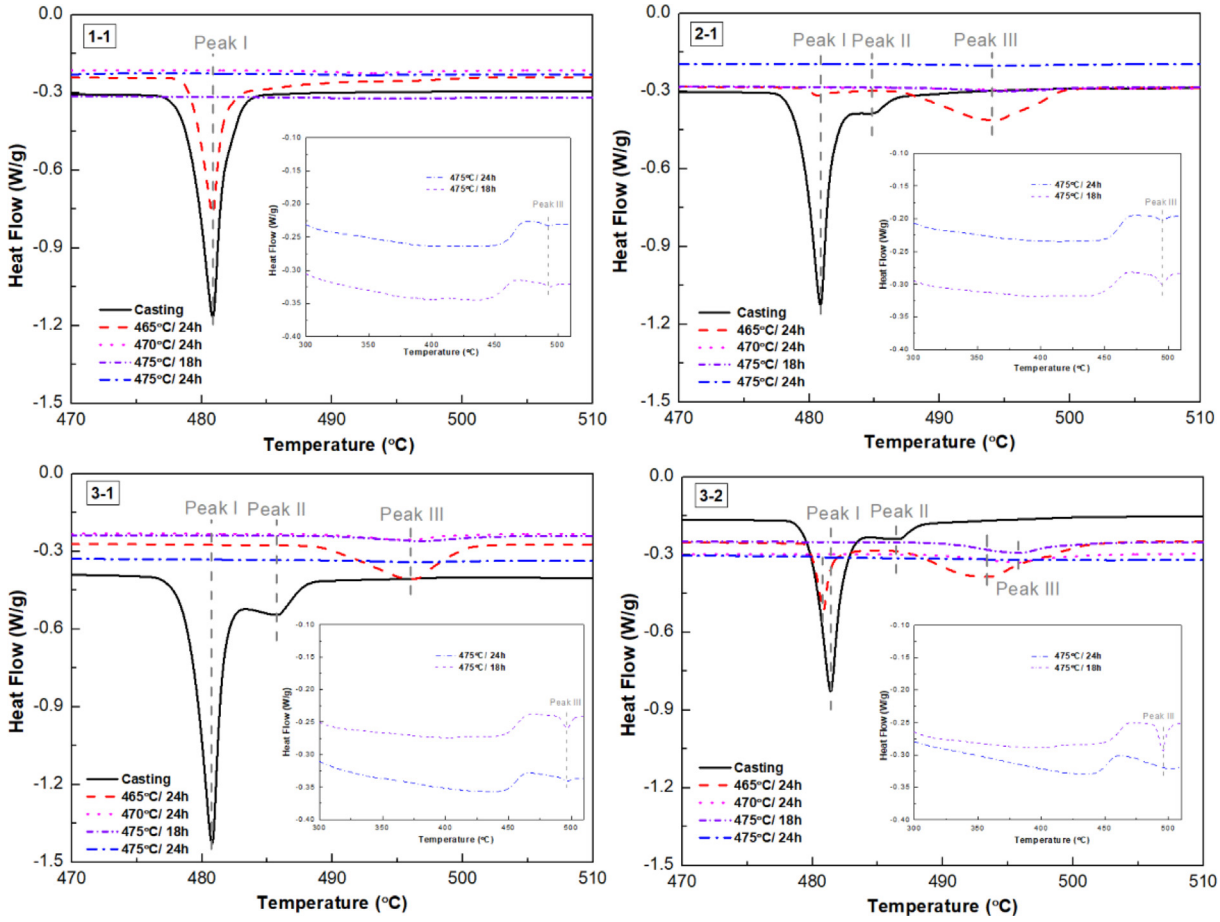

Fig. 4. DSC curves of the as-cast and homogenized (465 °C and 470 °C, 24 h and 475 °C, 18 h/24 h) alloys.

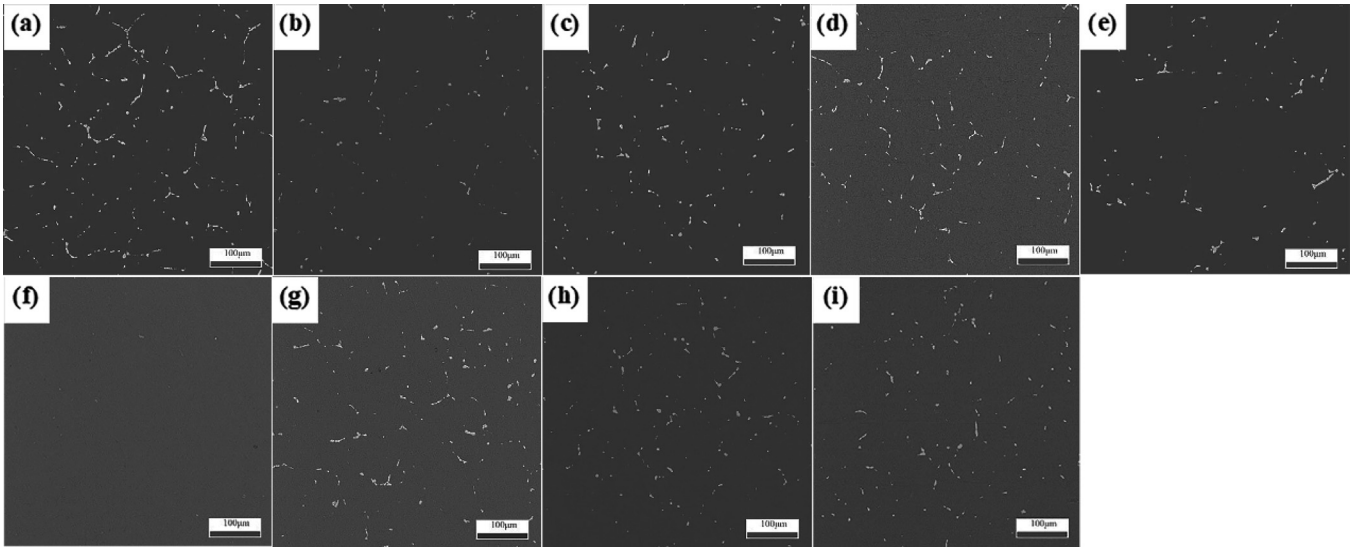

Fig. 5. SEM images of the two-step homogenized alloys 1-2, 2-2, 3-3 (a, b, c: alloy 1-2; d, e, f: alloy 2-2; g, h, i: alloy 3-3; a, d, g: 475 °C/24 h; b, e, h: 475 °C/24 h + 485 °C/12 h; c, f, i: 475 °C/24 h + 485 °C/24 h).

form of Al_6CuMg_4) [14,53]. It is noteworthy that the variable composition of the present Cu-enriched phase (Table S1, for example the stoichiometric ratio of the Cu-enriched [AlCuMgZn] phase, i.e., Mg:Al:Cu:Zn≈10: 65: 14: 10 in the alloy 1-2) is different from the stoichiometric *S* ($Al_2Cu_XMgZn_{1-X}$) [19], *M* ($Mg(ZnAlCu)_2$) [43] or *T* ($Mg_3(AlCuZn)_2$) phases [14]. Furthermore, the dissolution temperature of the new phase (between that of the *M* (~480 °C) and *S* (~490 °C) phases, corresponding to the endothermic peak II in Fig. 1(m)), reveals that a metastable phase (i.e., the Cu-enriched phase) appears in the as-cast state, namely the [AlCuMgZn] phase

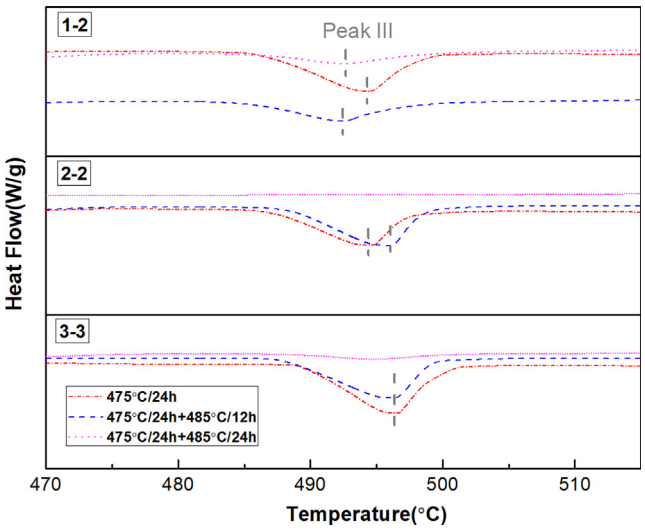

Fig. 6. DSC curves of homogenized (one- and two-step) alloys.

(the structural study is on-going), which is consistent with a previous report, i.e., existence of Cu-enriched non-equilibrium aluminides between the *S* and θ phase [42]. The above analysis considers no *S* phase but mainly α-Al, *M* and [AlCuMgZn] phases in the as-cast state, which is similar to the results calculated by the Scheil model (Fig. 7) except for the alloy 1-1. However, the solidification paths and phase components calculated by the Scheil model and the equilibrium phase diagram are not completely consistent with the experimental results, i.e., no θ phase appears in the Scheil model but in the equilibrium state, which agrees with the results in Table S1. The *T* phase presents in the Scheil model while the *M* phase can be found in the equilibrium state and experiments. Although the *V* phase calculated by the Scheil model is close to the Cu-enriched phase, the Scheil model shows that the *V* phase exists in the alloy 1-1, while the experiment and the equilibrium phase diagram show there is no Cu-enriched phase, which signifies that the *V* phase might be different from the Cu-enriched phase. In a word, the Schiel model can predict all possible phases during the solidification, but it is not consistent with the real solidification. The real solidification mostly agrees with the equilibrium solidification and usually falls between the Schiel model and equilibrium calculation. Finally, the phase components of different alloys are same (with different phase fraction) except for the alloy 1-1 without the Cu-enriched phase due to its low (Cu + Mg) content.

It is considered that the η phase can be formed for the alloys with Zn > 3.0 wt% and Zn:Mg > 2.2 [38], which agrees with the present alloys. The reaction heat ΔH_R of the endothermic peak I (corresponding to the area fraction of the *M* phase) in Fig. 1(m) is ranked as: 2-2 > 1-1 > 1-2 > 2-1 > 3-2 > 3-3 > 3-1 (Table 2), which is closely related to their Zn, Mg and Cu contents. The fraction of the *M* phase increases as the Zn:Mg ratio increases and (Cu + Mg) content decreases for the alloys 1-1, 2-1 and 3-1, which is consistent with previous study [14]. However, the fraction of the *M* phase depends on the (Zn + Mg + Cu) content for the alloys 3-1

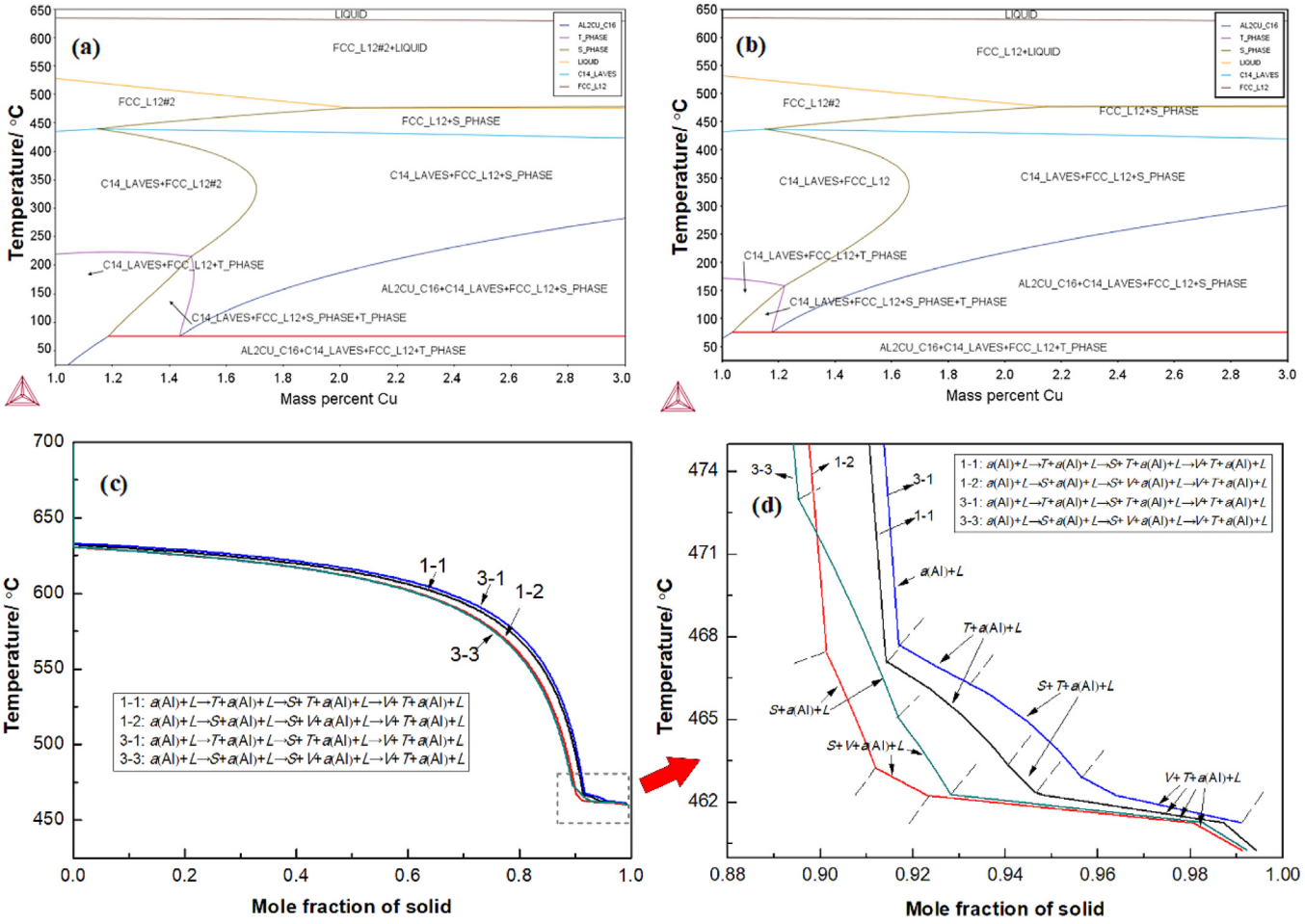

Fig. 7. Calculated isopleth((a): alloy 1-1; (b): alloy 1-2) and the solidification paths in the Scheil model[(c) and (d), alloys 1-1, 1-2, 3-1, 3-3].

Table 3
Solidification paths of different alloys under equilibrium condition.

alloys	Solidification process
1-1	$L \xrightarrow{635\,^{\circ}C} \alpha\text{-Al}+L \xrightarrow{470\,^{\circ}C} \alpha\text{-Al}+S \xrightarrow{435\,^{\circ}C} \alpha\text{-Al}+S+M \xrightarrow{167\,^{\circ}C} \theta+\alpha\text{-Al}+S+M \xrightarrow{75\,^{\circ}C} \theta+\alpha\text{-Al}+T+M$
1-2	$L \xrightarrow{635\,^{\circ}C} \alpha\text{-Al}+L \xrightarrow{475\,^{\circ}C} \alpha\text{-Al}+S \xrightarrow{425\,^{\circ}C} \alpha\text{-Al}+S+M \xrightarrow{270\,^{\circ}C} \theta+\alpha\text{-Al}+S+M \xrightarrow{75\,^{\circ}C} \theta+\alpha\text{-Al}+T+M$
2-1	$L \xrightarrow{635\,^{\circ}C} \alpha\text{-Al}+L \xrightarrow{473\,^{\circ}C} \alpha\text{-Al}+S \xrightarrow{435\,^{\circ}C} \alpha\text{-Al}+S+M \xrightarrow{338\,^{\circ}C} \alpha\text{-Al}+S+T+M \xrightarrow{75\,^{\circ}C} \theta+\alpha\text{-Al}+M+T$
2-2	$L \xrightarrow{635\,^{\circ}C} \alpha\text{-Al}+L \xrightarrow{476\,^{\circ}C} \alpha\text{-Al}+S \xrightarrow{422\,^{\circ}C} \alpha\text{-Al}+S+M \xrightarrow{183\,^{\circ}C} \theta+\alpha\text{-Al}+S+M \xrightarrow{75\,^{\circ}C} \theta+\alpha\text{-Al}+T+M$
3-2	$L \xrightarrow{635\,^{\circ}C} \alpha\text{-Al}+L \xrightarrow{475\,^{\circ}C} \alpha\text{-Al}+S+M \xrightarrow{376\,^{\circ}C} \alpha\text{-Al}+S+M+T \xrightarrow{305\,^{\circ}C} \alpha\text{-Al}+M+T \xrightarrow{180\,^{\circ}C} \alpha\text{-Al}+S+M+T \xrightarrow{75\,^{\circ}C} \theta+\alpha\text{-Al}+M+T$
3-3	$L \xrightarrow{635\,^{\circ}C} \alpha\text{-Al}+L \xrightarrow{478\,^{\circ}C} \alpha\text{-Al}+S+M \xrightarrow{251\,^{\circ}C} \theta+\alpha\text{-Al}+S+M \xrightarrow{75\,^{\circ}C} \theta+\alpha\text{-Al}+T+M$

and 3-2 with similar Zn:Mg ratio and (Cu + Mg) content, i.e., the higher the (Zn + Mg + Cu) content, the higher the fraction of *M* phase (Table S1). Additionally, it is known that the high Zn:Mg ratios and/or high Cu levels are conducive to forming the *M* phase [38,40], but excess Cu may cause coarse *S* phase that will consume Mg solute and decrease the fraction of the *M* phase [62]. The high Cu level can promote the formation of the *M* phase due to stoichiometric balance among Zn, Mg and Cu solutes (that means all the Zn, Mg and Cu atoms can be consumed to form the second phase without any excess) for the alloy 2-2 with medium Zn:Mg ratio compared with that of the alloy 1-1. The alloy 1-2 with high (Cu + Mg) content (excess Cu) and Zn:Mg ratio (=3.41) higher than the alloys 2-1, 3-1, 3-2 and 3-3 exhibits more *M* phase, while the alloy 3-3 with high (Cu + Mg) content (excess Cu) and Zn:Mg ratio (=3.02) close to that of the alloys 1-1 and 2-2 exhibits less *M* phase. Fig. 8 shows that the reaction heat ΔH_R (peak II) is closely related with the alloy's (Mg + Cu) contents: the higher the (Mg + Cu) content, the higher the reaction heat, and the higher the fraction of the [AlCuMgZn] phase, which is similar with the relationship between the (Mg + Cu) level and *S* phase content [14,19]. Thus, the [AlCuMgZn] phase does not exist in the as-cast alloy 1-1 but in others with (Mg + Cu) level above 4.04-4.08 wt%. Also, the formation of the θ phase mainly depends on Cu and Mg levels (or Cu:Mg ratio) but not on Zn level [40], i.e., high Cu:Mg ratios can facilitate the formation of θ phase [38]. As a result, it is easier for the alloys 1-2 and 3-3 but difficult for the alloys 2-1, 3-1 and 3-2 to form θ phase (Table 1), which agrees with their as-cast microstructures (Fig. 1 (g, h, i)).

Fig. 9 shows the variation of the Zn:Mg ratio and (Mg + Cu) content as well as related phase components in the as-cast alloys. It reveals that the alloys with high Zn:Mg ratio and low (Mg + Cu) content (such as AA7085 [63,64], AA7037 [63,65] and AA7056

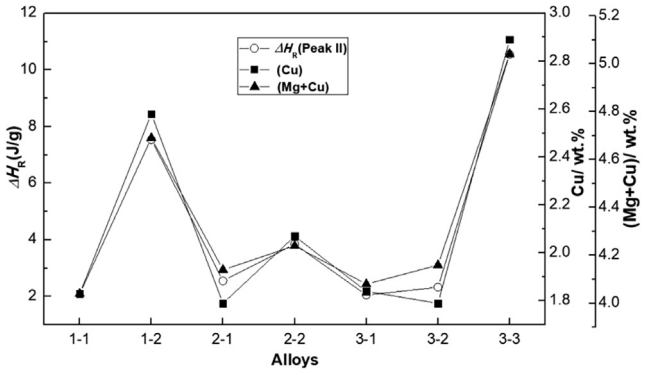

Fig. 8. Reaction heat ΔH_R (peak II) and the correlation of ΔH_R and (Mg + Cu) content of different alloys.

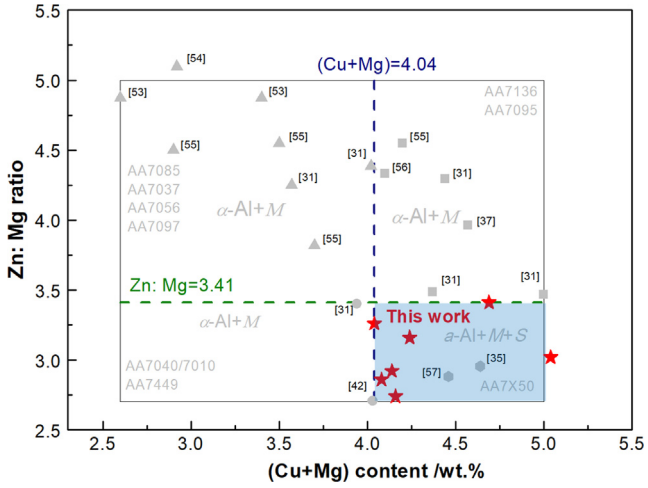

Fig. 9. Analysis of solidification microstructure of previous and current studied alloys with different Zn:Mg ratio and (Cu + Mg) content.

[21,43,65], AA7097 [65] alloys) mainly contain α-Al and *M* phase but the alloys with low Zn:Mg ratio and high (Mg + Cu) content (such as AA7x50 alloy [47,66] and the present alloys) mainly contain α-Al, *M* and *S* or Cu-enriched phases. However, the as-cast alloys only contain α-Al and *M* phases for low Zn:Mg ratio and low (Mg + Cu) content (such as AA7040/7010 [54], AA7449 [43] alloy), or for high (Mg + Cu) content and high Zn:Mg ratio (such as AA7136 [43], AA7095 [65] alloys). The alloys with high Zn:Mg ratios do not contain the Cu-enriched phase or *S* phase for equal (Mg + Cu) content, such as the alloys 2-2 and 3-1, AA7095 [65] (Al-9.1Zn-2.0 Mg-2.2Cu, wt%) and AA 7A56 [21] (Al-9.0Zn-2.1 Mg-2.0Cu, wt%) alloys. It can be found that the as-cast alloys mainly contain α-Al and *M* phases except for the blue area that may contain additional Cu-enriched or *S* phase (Fig. 9).

The fraction of the η phase increases with Zn content but decreases with Mg content for Zn <= 6.9 wt% for the alloys with different Zn, Mg and Cu contents (6.5–8.0 wt% Zn, 1.8–2.6 wt% Mg and 1.5–3.0 wt% Cu), as shown in Fig. 10(a, b, c, i, j), indicating that this fraction increases with Zn:Mg ratio. However, the fraction increases firstly and then decreases with Mg content for Zn > 6.9 wt%, and the Mg content corresponding to the maximum fraction of the η phase gradually increases for higher Zn content. The alloys can be divided into three types: 6.5–6.9 Zn wt%, 7.2–7.6 Zn wt% and 7.8–8.0 Zn wt% based on the Zn and Mg content corresponding to the maximum η fraction (Fig. 10(j)), which corresponds to Mg<= 1.8 wt%, Mg = 2.0 wt% and Mg = 2.2 wt%, respectively (Fig. 10(k)), and the related Zn:Mg ratios are ≥3.6–3.83 (6.5–6.9 wt% Zn), 3.6–3.8 (7.2–7.6 wt% Zn) and 3.55–3.64 (7.8–8.0 wt% Zn). It seems that there is a critical Zn:Mg ratio corresponding to maximum fraction of the η phase, as schematically shown in Fig. 10(l), below which the fraction increases with Zn:Mg ratio but decreases above this critical ratio that is consistent with previous study [67]. The Zn:Mg ratios in this study are lower than above critical values (~3.6), thus as the Zn:Mg ratio increases, the fraction of the η phase increases. The analysis is based on the consideration that the low Cu content (1.5 wt%) has no obvious effect on the fraction of the η phase (Fig. 10(d)). Although it could affect the formation of the *M* phase and the corresponding Mg content as well as critical Zn:Mg ratio under higher Mg and Cu contents, the critical Zn:Mg ratio can still hold. It is noted that higher Cu content will reduce the solubility of the Mg solute, thus decreasing the fraction of the η phase (Fig. 10(d)), which is in accord with the present alloys (such as the alloys 1-1, 2-2 and 3-3). Fig. 10(e, f, g, h) show that

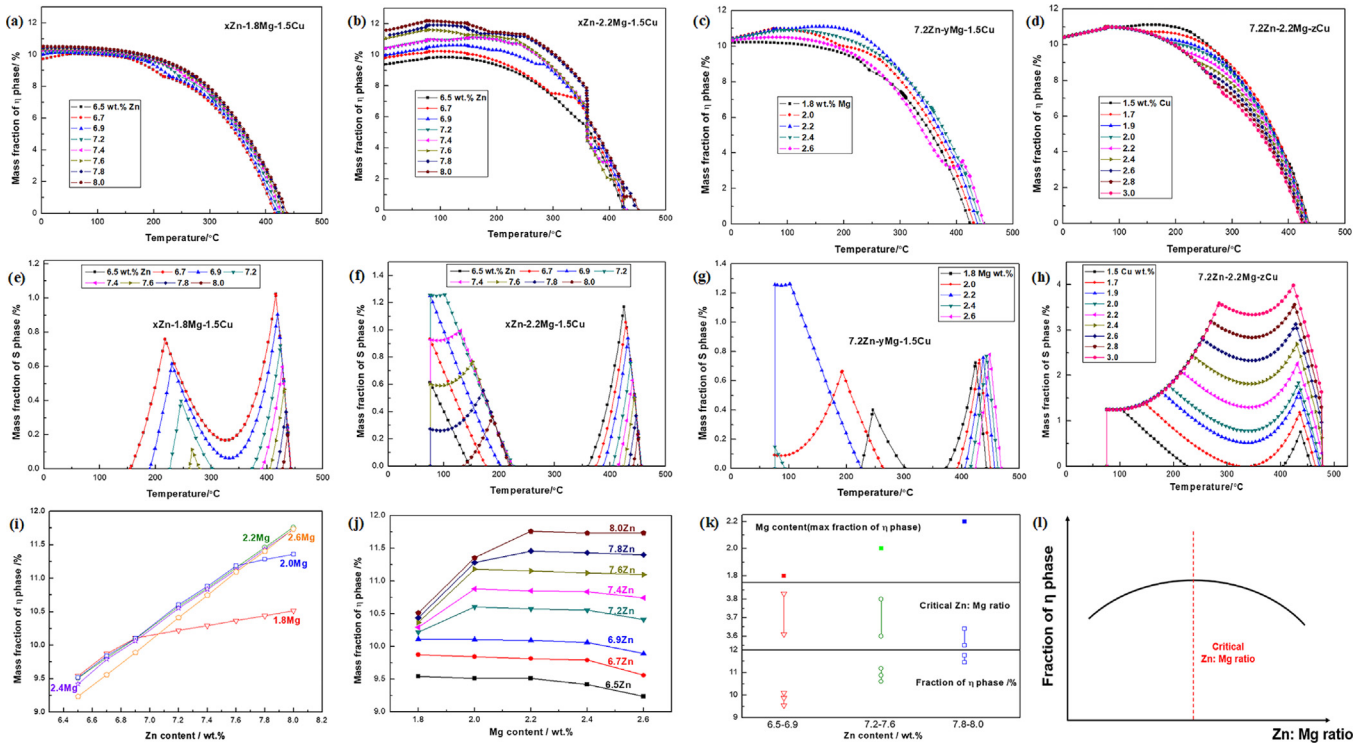

Fig. 10. The fraction of η and S phases under different Zn (a, b, e, f), Mg (c, g) and Cu contents (d, h). (i, j) the fraction of η phase fraction at different Zn and Mg contents at room temperature (24 °C); (k) the critical Zn:Mg ratios and Mg content corresponding to the maximum fraction of η phase at different Zn contents; (l) schematic variation of the fraction of η phase with Zn:Mg ratio.

there is no S phase after the solidification, which is in line with the results in Fig. 1 and Table S1. However, the M and Cu-enriched [AlCuMgZn] phases can evolve into stable S phase during high-temperature treatment (or homogenization) (Fig. 2 and Table S3), which is the results from the different diffusion velocity of the Zn, Mg and Cu atoms during high temperature treatment, i.e., the Zn atom in the M and Cu-enriched [AlCuMgZn] phases is diffused into the matrix more easily than the Mg and Cu atoms, finally leading to the transformation from the M and and Cu-enriched [AlCuMgZn] phases to the S phase [42,54,61]. The residual S phase after high-temperature treatment (or homogenization) could be detrimental to the alloy's integrated properties, and it's important to avoid the residual S phase by tuning the composition (Zn/Mg/Cu), so the evolution of the S phase fraction for the alloys with different compositions (Zn/Mg/Cu) at high temperature during solidification were discussed based on the one-axis equilibrium thermodynamic calculations in order to guide the alloy design (Zn:Mg ratio and (Cu + Mg) content). The varied Zn (for Zn = 6.5–8.0 wt%, Mg = 1.8 or 2.2 wt%, Cu = 1.5 wt%) and Mg contents (for Zn = 7.2 wt%, Mg = 1.8–2.6 wt%, Cu = 1.5 wt%) have less effect on the S phase during the solidification (Fig. 10(e, f, g)), but higher Zn:Mg ratio is conducive to decrease the fraction of the S phase (Fig. 10(e, f, g)). Also, the Cu content (for Zn = 7.2 wt%, Mg = 2.2 wt%, Cu = 1.5–3.0 wt%) has a significant influence on the formation of the S phase, i.e., the maximum S phase fraction increases from 1% to 4% (Fig. 10(h)). Thus, the Cu content should be strictly controlled to avoid more S phase, especially under higher Mg content (2.0–2.4 wt%). The S phase can be basically dissolved by high-temperature treatment for Cu = 2.07 wt% (the alloy 2-2), but will be residual for Cu > 2.07 wt% (i.e., the alloys 1-2 and 3-3). The fraction of the η phase can be maximized with critical Zn:Mg ratio and lower (Cu + Mg) content, while the S phase can be avoided by increasing the Zn:Mg ratio and decrease the (Cu + Mg) content.

4.2. Homogenization kinetic analysis

The isothermal equilibrium phase diagrams in Fig. 11 show that the alloys 1-1, 2-1, 3-1 and 3-2 are located in the α-Al + S phase field at 470 °C but in the single α-Al phase field at 475 °C, which could suggest a homogenization temperature of 475 °C with considering the dissolution of the M phase (Fig. 1(m)). However, the alloys 2-2, 1-2 and 3-3 are located in the α-Al + S phase field at 475 °C and may be overburnt at 480 °C. It also shows that the alloy 2-2 near the solvus of the S phase while the alloys 1-2 and 3-3 far away from this solvus, and longer soaking time or two-step homogenization process (low + high temperatures) might be suitable, especially the latter. The homogenization process for the alloy 2-2 is suggested as 475 °C/24 h + 485 °C/24 h, but a complete dissolution of the second phases after this two-step homogenization for the alloys 1-2 and 3-3 cannot be achieved because of the residual S phase, which could be costly eliminated with higher homogenization temperatures or longer times from the SEM observation and DSC analysis (Figs. 5 and 6, Table S5 and S6).

The dissolution of the M and [AlCuZnMg] phases, the transformation of the M and [AlCuZnMg] phases to S phase [54,55] (i.e., Zn < 8 wt%) and the dissolution of the S phase [36,59,68] could be occurred during the homogenization. Firstly, the interdendritic eutectic microstructures (i.e., M and [AlCuZnMg] phases) are dissolved during the homogenization but the transformation into the S phase as well as the growth of the S phase mainly depends on the diffusion of solute atoms from these eutectic phases [49]. It is found that high Cu concentration might be formed in local eutectic regions for the low diffusion rate of Cu atom compared to that of Zn and Mg atoms [69] and this may facilitate the formation of the S phase [59]. Further homogenization will continue the transformation into the S phase and dissolve the eutectic microstructures, and the decrease of the Cu concentration gradient between grain boundaries and Al matrix will promote the dissolu-

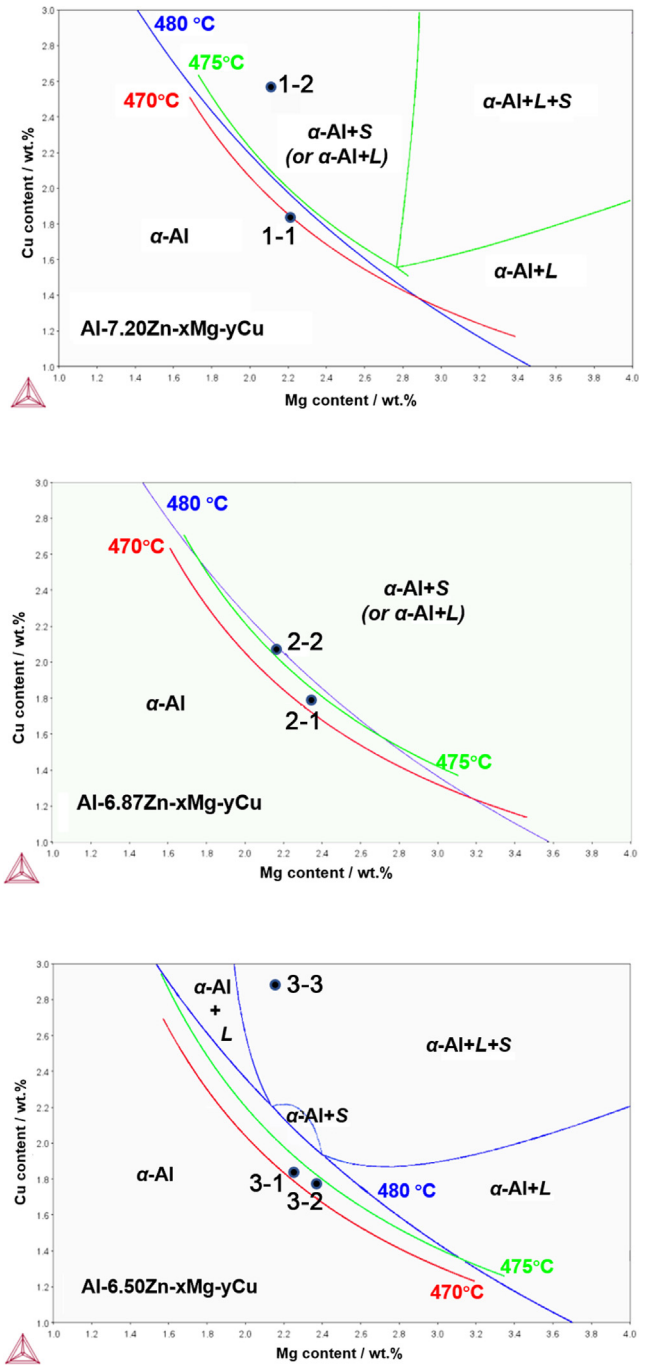

Fig. 11. Calculated isothermal sections of Al-(7.2 wt%, 6.87 wt%, 6.5 wt%)Zn-Mg-Cu system at 470 °C, 475 °C and 480 °C.

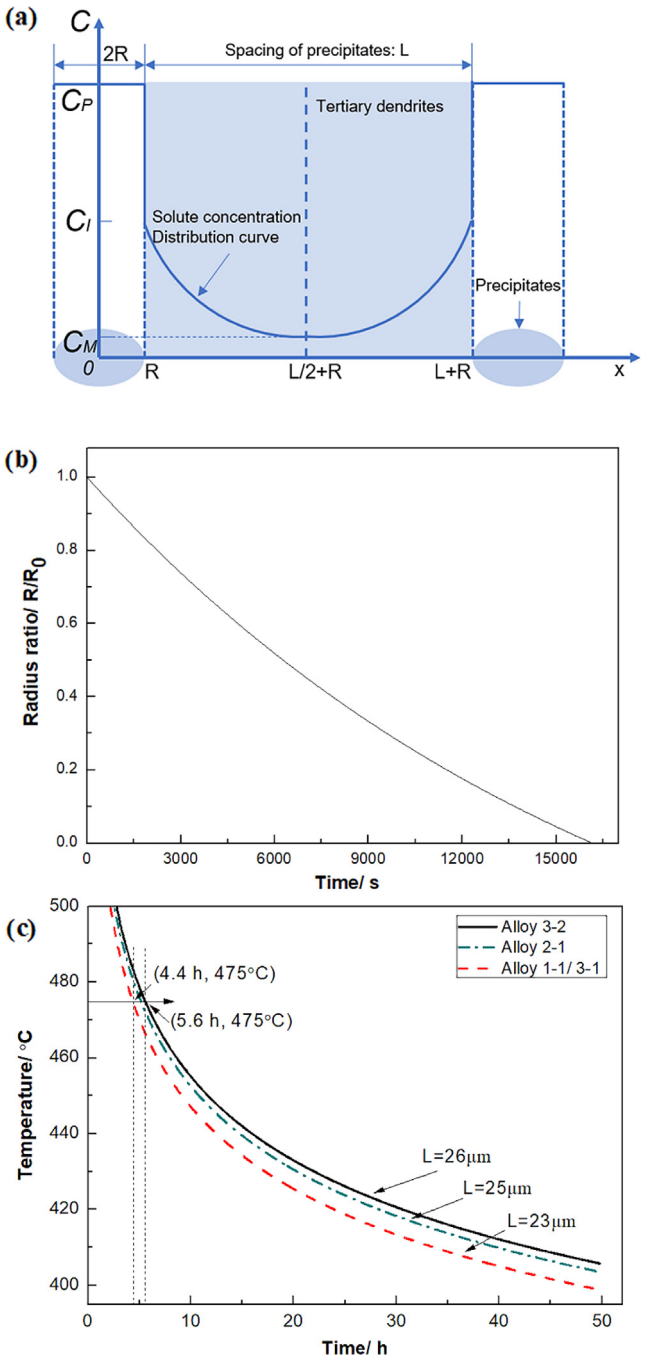

Fig. 12. (a) Schematic diagram of the solute concentration distribution between the tertiary inter-dendrite phases in the initial state; (b) Dissolution rate curves of the tertiary inter-dendrite phase at 475 °C; (c) Diffusion kinetic curves of solute elements in the tertiary inter-dendrites phase.

tion of the *S* phase [49,59]. However, the different dissolution behaviour of the intragranular /intergranular phase during the homogenization should be considered.

(1) Kinetic analysis of intragranular phase dissolution and solute diffusion

The diffusion from the interdendritic second phases into Al matrix is considered as a planar diffusion process for the typical dendrite morphologies along with interdendritic second phases (i.e., *M* and Cu-enriched [AlCuZnMg] phases) in the as-cast alloys [70,71]. Supposing a spherical second phase, the initial solute distribution is schematically shown in Fig. 12.

Where

$2R$ is the diameter of the interdendritic second phase,
L is the distance between the interdendritic second phase, which is equal to the dendrite arm spacing,
C_P is the average solute concentration inside the phase,
C_I is the average solute concentration at the interface between the phase and dendrite,
C_M is the average solute concentration in the matrix at $L/2$ position.

A stationary interface and homogeneous solute concentration within the phase are generally considered without variation of the distance or time, and the solute concentration at the interface is not changed during the diffusion.

Solute concentration distribution curve in the dendrites shown in Fig. 12(a) is as follows[70,71]:

$$C_{(x,\ t)} = C_M + (C_I - C_M)[1 - \sin[\frac{\pi(x-R)}{L}] \cdot exp[-\frac{\pi^2}{L^2}Dt]] \quad (1)$$

The dissolution rate dR/dt of the second phase between dendrites can be expressed as[70,71]:

$$\frac{dR}{dt} = -\frac{Dk\pi}{2L} \cdot exp(-\frac{\pi^2}{L^2}Dt) \quad (2)$$

The k value is related to the solute concentration and expressed as $k = \frac{2(C_I - C_M)}{C_P - C_I}$. Similar to the grain boundary phases, the intragranular phase mainly consists of the M phase along with the Cu-enriched [AlCuMgZn] phase and a few θ phase. Therefore, with considering the different Cu concentrations in the grain boundary phases, the Cu concentration for the calculation was averaged from the M phase, the Cu-enriched [AlCuMgZn] phase and θ phase. The approximative Cu concentration of the interdendrite phases (C_P) close to the average Cu concentration of the grain boundary phases (i.e., ~20 at.% obtained from the Table S1 and Fig. 1(k)). The Cu concentration in the dendrite is 0 ~ 3 at.% and C_M = 1 at.% is used based on the line scan analysis ((Fig. 1(k))). It is assumed that the average Cu concentration at the interface (C_I) is the middle value (~11 at.%) between the average solute concentration inside the phase (C_P) and the average solute concentration in the matrix at $L/2$ position (C_M) based on the line analysis results (Fig. 1(k)). Thus, k equals to 2 and is not affected by Cu concentration.

The radius evolution of the second phase with diffusion time by integrating the Eq.(2) to the diffusion time t can be described as [70,71]:

$$\frac{R}{R_0} = 1 + \frac{kL}{2\pi R_0}\left[exp\left(-\frac{\pi^2}{L^2}Dt\right) - 1\right] \quad (3)$$

where R_0 is the initial radius of the second phase. Statistics show that in the alloys 1-1, 2-1, 3-1 and 3-2, R_0 is<5 μm, and the spacing is less than 26 μm. Then, the calculated radius at 475 °C in Fig. 12(b) indicates the radius ratio (R/R_0) is gradually decreased with homogenization times and tend to be zero after ~4.5 h, i.e., the interdendrite phase is dissolved completely after 4.5 h homogenization.

In addition to the dissolution of second phase, a uniform solute distribution is also required. The concentration difference between two phases will be gradually decreased with prolonging the homogenization times. Supposing 1% difference corresponds to uniform solute diffusion, the related condition can be expressed as[71]:

$$\frac{\Delta C_{(t)}}{\Delta C_{(0)}} = \frac{C_{(R,t)} - C_{(\frac{L}{2}+R,t)}}{C_{(R,0)} - C_{(\frac{L}{2}+R,0)}} = 1\% \quad (4)$$

Based on the Eq. (1), Eq. (4) can be simplified as:

$$exp\left(-\frac{\pi^2}{L^2}Dt\right) = 1\% \quad (5)$$

The kinetic equation of solute diffusion process can be obtained by substituting Arrhenius equation ($D = D_0 \cdot \exp(-\frac{Q}{RT})$) into Eq. (5) [71]:

$$\frac{1}{T} = \frac{R}{Q}\ln\left(\frac{4\pi^2 D_0 t}{4.6L^2}\right) \quad (6)$$

The diffusion kinetic curves of Cu solute with different spacings are shown in Fig. 12(c) and it can be found that the smaller spacing corresponds to shorter time and/or lower temperature for uniform diffusion. The times for uniform solute diffusion for the alloys 1-1, 2-1, 3-1 and 3-2 with L = 23-26 μm at 475 °C are 4.4–5.6 h.

(2) Kinetic analysis of intergranular phase dissolution and solute diffusion

It can be found that the dissolution times of the intragranular second phase and for the uniform solute diffusion are relatively short at 475 °C combined with above analysis about the dissolution of intragranular second phases and solute diffusion kinetics. But longer times might be required for dissolving the eutectic structures and second phases as well as solute diffusion at some temperatures (such as 475 °C) [70,71]. It is known that α-Al + M and [AlCuZnMg] eutectic structures appear at grain boundaries along with a few α-Al + θ eutectic or θ and Al_7Cu_2Fe phases. Partial eutectic phases are rapidly dissolved as well as some θ phase but without the dissolution of Al_7Cu_2Fe and S phases during the homogenization. The dissolution and/or transformation of the M, [AlCuZnMg] and S phases can be theoretically defined as a diffusion process in a semi-infinite space [71]. In order to simplify the calculation and analysis, the grain boundary residual phase is assumed to be spherical and Fig. 13(a) shows the initial solute concentration. The distribution curve of solute concentration during the diffusion can be expressed by Fick's second law containing Gauss error function [71]:

$$C_{(x,\ t)} = C_M + (C_I - C_M)\left[1 - \frac{r}{x}erf\frac{(x-r)}{2\sqrt{Dt}}\right] \quad (7)$$

where r is the radius of grain boundary phase, x is their spacing.

The dissolution rate of grain boundary phase is expressed as follows based on the equilibrium solute flux at the phase interface [71]:

$$\frac{dr}{dt} = -\frac{k}{2}\left(\frac{D}{r} + \sqrt{\frac{D}{\pi t}}\right) \quad (8)$$

Then, the size evolution of the phase with homogenization time by integrating Eq. (8) with time t can be expressed as [71]:

$$\frac{r}{r_0} = 1 - \frac{kDt}{2r_0^2} - \frac{k}{r_0}\sqrt{\frac{Dt}{\pi}} \quad (9)$$

The dissolution rate curves of grain boundary phases with different sizes at 475 °C based on the Eq. (9) are shown in Fig. 13 (b). It shows that the dissolution time increases rapidly with the size (i.e., 10–20 μm) and is 4.0–16.1 h with the maximum less than 25.2 h, being consistent with experimental results (Figs. 2 and 4).

It will take times to eliminate the concentration difference between the grain boundary and grain interior considering the higher solute concentration near grain boundaries. It is assumed that the solute concentration distribution in the grains can be expressed as a sine function, which will be gradually attenuated with the increase of homogenization times [55]. It means that this concentration difference will be decreased gradually. The concentration distribution [71] can be expressed in a similar form to Eq. (1).

$$C_{(x,\ t)} = C_{in} + (C_{gb} - C_{in})[1 - \sin[\frac{\pi x}{d}] \cdot exp[-\frac{\pi^2}{d^2}Dt]] \quad (10)$$

Where

C_{in} are the solute concentrations within grains,
C_{gb} are the solute concentrations at grain boundary,
x is the distance from the grain boundaries,
d is the half distance of adjacent grain boundary phase.

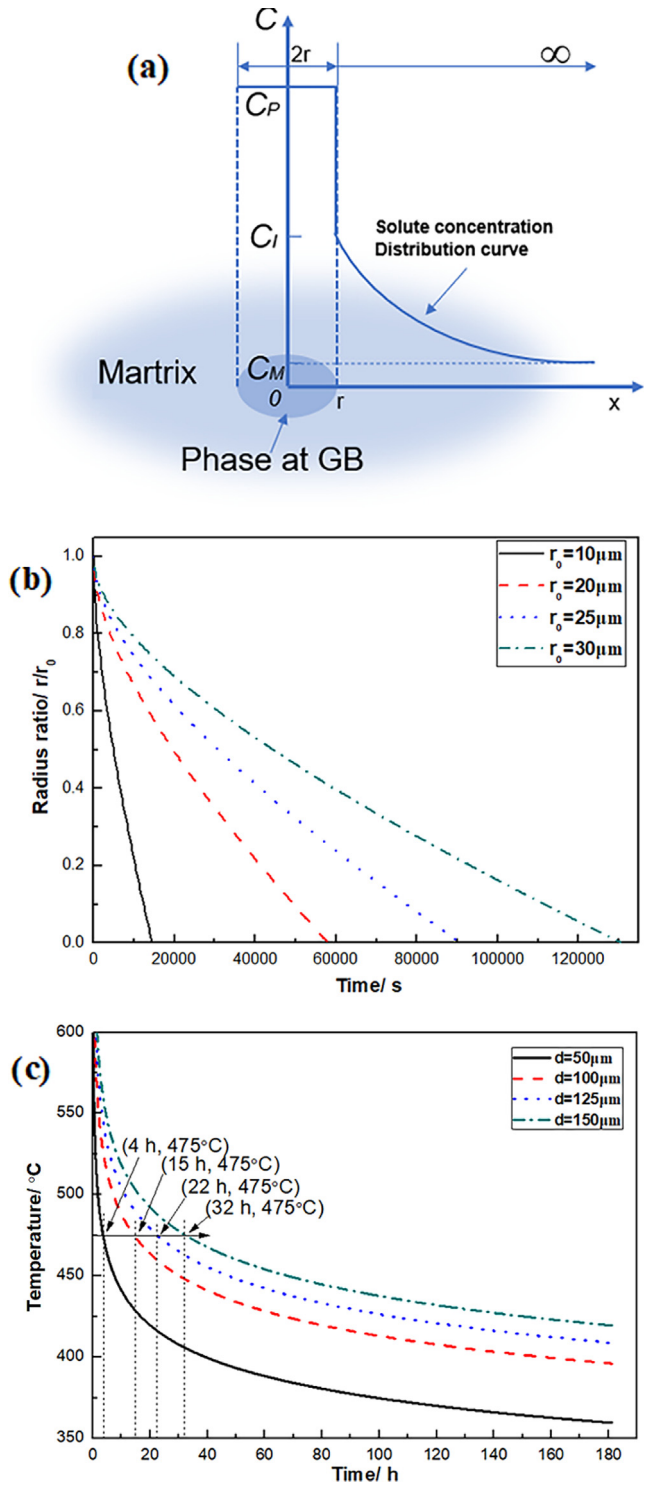

Fig. 13. (a) Schematic diagram of initial solute concentration distribution around grain boundary phase; (b) Dissolution rate curves of phase at grain boundary; (c) Diffusion kinetic curves of solute at the grain boundary.

The solute diffusion becomes uniform when the concentration difference decreases to 1% relative to the initial state. The kinetic diffusion equation can be expressed as[7]:

$$\frac{1}{T} = \frac{R}{Q} \ln\left(\frac{4\pi^2 D_0 t}{4.6d^2}\right) \tag{11}$$

The diffusion kinetic curves of Cu solute with different spacings of adjacent grain boundary phase based on Eq. (11), are shown in Fig. 13(c), revealing that the smaller the spacing, the less the diffusion time. A uniform solute diffusion at 475 °C requires 4–32 h for the spacing of 50–150 μm, in accord with above results (Fig. 2 and Table S2 and S4). As a result, the element distribution will become uniform after 475 °C – 24 h homogenization except for the residual insoluble phase at grain boundaries.

4.3. Regulating principle for composition and phase component

The above reveals that the maximum allowable treatment temperature, 475 °C, corresponds to the maximum solubility limit that depends on temperatures for the low-to-medium Zn content (6.5–7.2 wt%) (Fig. 11). According to the solubility curves from 450 °C to 500 °C[72] or the isothermal phase diagram at 475 °C (Fig. 11) and the phase stability in the Al-Mg-Cu-Zn system at 460 °C[73], the present alloys 1-1, 2-1, 3-1 and 3-2 are within the α-Al phase field while the alloy 2-2 is in the (α-Al + *S*) phase field at 475 °C, but both will be overburnt at 480 °C or above. As a result, the one-step homogenization should be performed at or below 475 °C for the alloys 1-1, 2-1, 3-1 and 3-2 (Fig. 2 (a, c, e, f)), however, the *S* phase is residual in the alloy 2-2 (Fig. 2 (d)) that is in the region below the solvus of the *S* phase at 480 °C (Fig. 11). Thus, this alloy can be treated by the two-step homogenization process: the first low-temperature homogenization at or below 475 °C can dissolve the *M* and Cu-enriched phases including partially transformation into the *S* phase, and then, the full homogenization can be achieved at higher temperature, i.e., 475–490 °C (Fig. 5 (d, e, f)). But the alloys 1-2 and 3-3 in the region above the solubility limit of the *S* phase at 490 °C cannot be completely homogenized even at higher temperatures (Fig. 5 (a, b, c) and (g, h, i)).

Fig. 14(b) shows the schematic solubility limits of the alloys with low-to-medium Zn content (5.47–7.24 wt%) at different temperatures and three regions are separated by two critical solubility limits at 475 °C and 490 °C: region 1 – below 475 °C, region 2 – between 475 °C and 490 °C, and region 3 – above 490 °C. For the alloys in the region 1, the second phase can be fully dissolved after the one-step homogenization (at 475 °C or below), but for the alloys in the regions 2 and 3, the second phase cannot be fully dissolved after the one-step homogenization at 475 °C or below and overburn may occur at higher temperatures, i.e., 475–490 °C, and a two-step homogenization process could be used. As a result, the homogenization process for the alloys with low-to-medium Zn content can be designed based on the principle of solubility limit. However, completely eliminating the coarse phases (i.e., *S* phase) after high-temperature treatment for the alloys with narrow (such as alloy 2-2) or no α-Al single phase field (such as alloys 1-2 and 3-3) is still difficult. And the high solvus of the *S* phase will increase the quenching sensitivity and subsequently affect the strength, toughness, and SCC performance[4,5]. Therefore, a reasonable composition design should follow the basic principle[4] of low *S* phase solvus and wide α-Al single phase field, and those with narrow or no α-Al single phase field and high *S* phase solvus should be avoided [6,13,74].

In this study, the fraction of the *S* phase after homogenization at 475 °C for 24 h mainly depends on the (Cu + Mg) content, i.e., high (Cu + Mg) content will cause more *S* phase (Fig. 2 and Table S2), which is consistent with previous studies [13,14]. Thus, the present alloys can be divided into three types according to the (Cu + Mg) content:

(1) low (Cu + Mg) content (4.04–4.16 wt%), i.e., the alloys 1-1, 2-1, 3-1 and 3-2, in which the *S* phase transformed from the *M* and Cu-enriched phases can be fully eliminated after 475 °C/24 h homogenization;

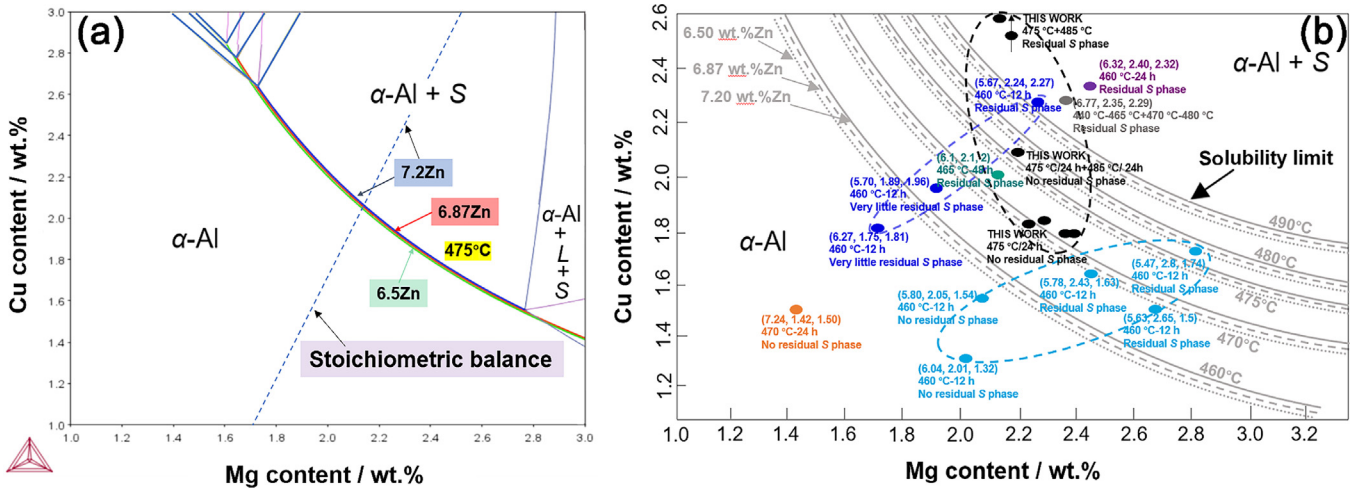

Fig. 14. (a) Equilibrium isothermal phase diagram of Al-Zn-Mg-Cu alloys with different Zn contents (6.5 wt%, 6.87 wt% and 7.2 wt%) at 475 °C; (b) Schematic solubility limit of Al-(6.5–7.2 wt%)Zn-xMg-yCu alloys at different temperatures.

(2) medium (Cu + Mg) content (~4.24 wt%), i.e., the alloy 2-2, in which abundant of the *S* phase transformed from the *M* and Cu-enriched phases can be eliminated after the homogenization of 475 °C/24 h + 485 °C/24 h;
(3) high (Cu + Mg) content (4.69–5.04 wt%), i.e., the alloys 1-2 and 3-3, in which the *S* phase transformed from the *M* and Cu-enriched phases cannot be completely eliminated after the two-step homogenization (475 °C/24 h + 485 °C/24 h).

Obviously, there is a critical (Cu + Mg) content near 4.24 wt%, below which the second phases can be completely dissolved after the homogenization at 475 °C, i.e., for the alloys 1-1, 2-1, 3-1 and 3-2, or the alloys in the α-Al single phase field or below the solubility limit at 475 °C. For the (Cu + Mg) content higher than this critical value or the alloys in (α-Al + *S*) phase field (i.e., the alloys 2-2, 1-2 and 3-3), there are still some residual coarse phases after high-temperature treatment (i.e., 475 °C) when the alloys lie outside the solubility limit at 490 °C (i.e., the alloys 1-2 and 3-3). However, these coarse phases can be completely dissolved after specific treatments (i.e., the two-step high-temperature treatment) when the alloys lie between the solubility limits at 475 °C and 490 °C (i.e., the alloy 2-2), but they may exhibit high quenching sensitivity[4,13,14]. Also, the Zn:Mg ratio can affect the fraction of the *S* phase, i.e., as the Zn:Mg ratio increases at a constant Cu content, the alloy will move from the two-phase field into a single-phase field[43]; high Zn:Mg ratio may increase the Cu solubility and more *S* phase can be dissolved[14], i.e., the AA7050 alloy. As a result, the fraction of the *S* phase after 475 °C/24 h homogenization will decrease with lowering the (Cu + Mg) content and/or increasing the Zn:Mg ratio. The effects of a range of Zn:Mg ratios (i.e., 3.5–5, presently 2.74–3.41) on the microstructure evolution needs more studies for reasonably matching the composition and homogenization process for advanced Al-Zn-Mg-Cu alloys.

For the critical (Cu + Mg) content, ten data (C_{Mg}, C_{Cu}) from the solvus in Fig. 14(a) are fitted and the minimum critical (Cu + Mg) content and the corresponding Cu and Mg contents are obtained by taking the derivative for a constant Zn content, as shown in Fig. 15(a), and it is slightly increased from 4.16 to 4.2 wt% with Zn content (6.5–7.2 wt%). For the negative effect of the alloy composition beyond the solubility limit line on the toughness[8,31], the solubility limit at 475 °C can be approximated as a linear function according to the minimum critical (Cu + Mg) content for the low-to-medium Zn alloys (6.5–7.2 wt%). For example, the solubility limit at 475 °C for Zn = 6.5 wt%, 6.87 wt% and 7.2 wt% can be defined as (C_{Mg} + C_{Cu}) = 4.16 wt%, (C_{Mg} + C_{Cu}) = 4.18 wt%, and (C_{Mg} + C_{Cu}) = 4.2 wt%, respectively. Therefore, for Zn = 7.2 wt%, the homogenization process can be preliminarily determined according to the relationship between the (Cu + Mg) content and 4.2 wt% (Fig. 15(b)), which means that the second phases (i.e., *M*, *T* and transformed *S* phases) can be fully dissolved at 475 °C or below in the alloys with (C_{Mg} + C_{Cu}) < 4.2 wt%. For the alloys with (C_{Mg} + C_{Cu}) > 4.2 wt%, most of the *M* and *T* phases can be fully dissolved after the one-step homogenization at 475 °C or below, but some of them might be transformed into the *S* phase that cannot be fully dissolved, for which a two-step homogenization process can be used. For the alloys with (C_{Mg} + C_{Cu}) ≫ 4.2 wt%, the *S* phase cannot be fully dissolved after high-temperature treatment and these alloys should be avoided.

For higher Zn-containing alloys, the isothermal equilibrium phase diagrams in Fig. 15(c) indicates that the overburn may occur above 460 °C and the homogenization temperatures should not be over 460 °C. The dissolution of the *M* and/or *T* phase and the reduction or elimination of solute segregation can be achieved after a one-step homogenization (at 460 °C or below) and there is no transformation of the *M* and/or *T* phase into the *S* phase for the high-Zn alloys (>8.0 wt%)[49,55]. Accordingly, the upper limit of the homogenization temperature for high Zn-containing alloys will not be increased after a low-temperature homogenization ((at 460 °C or below) and the acceptable homogenization temperature is still lower than the dissolution temperature of the *M* and/or *T* phase (~470 °C – 480 °C)[41]. Besides of dissolving second phases, the homogenization process can affect the formation of dispersoids such as size, number density, etc., however, which is not considered presently but only the coarse second phase and solute segregation. The corresponding solubility curve or maximum solubility limit at 460 °C is related to the critical (C_{Mg} + C_{Cu}) content (red-dotted line in Fig. 15(c)): 3.4–3.8 wt% for Zn = 8.5–10.0 wt%, lower than ~4.2 wt% for Zn = 6.5–7.2 wt%. This small variation (~0.4 wt%) of the critical (C_{Mg} + C_{Cu}) content for higher Zn-containing alloys (Zn = 8.5–10.0 wt%) agrees with the slight effect of the Zn content to the critical (C_{Mg} + C_{Cu}) content. As a result, with low (C_{Mg} + C_{Cu}) content (≤3.5 ~ 3.8 wt%), the solvus of coarse phases can be decreased and the α-Al phase field can be extended for high-Zn alloys compared with the high (C_{Mg} + C_{Cu}) content (>3.5 ~ 3.8 wt %) (Fig. 15(c)), which will facilitate the dissolution of coarse phases and decrease the quenching sensitivity (without considering the effects of dispersoids), i.e., AA7056 alloy. Furthermore, the solvus of the coarse phase will increase along with narrowed α-Al single

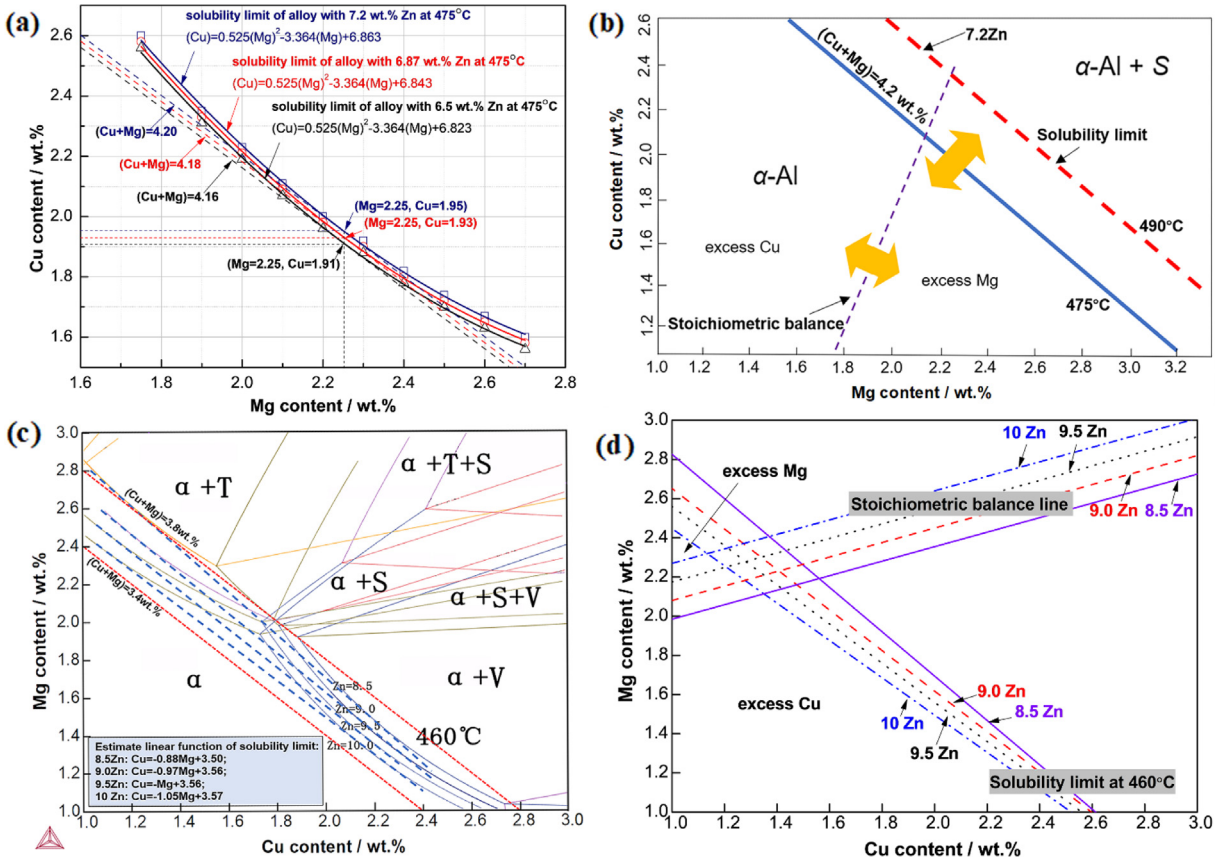

Fig. 15. (a) a critical (Cu + Mg) content determined by the solubility limit of alloys with different Zn content at 475 °C; (b) solubility limit of Al-7.2Zn-Mg-Cu alloys at 475 °C and 490 °C; (c) calculated isothermal section; (d) estimate and analysis of solubility limit and stoichiometric balance line of Al-Zn-Mg-Cu system with various Zn contents (8.5 wt%, 9.0 wt%, 9.5 wt% and 10 wt%) at 460 °C.

phase field for the (C_{Mg} + C_{Cu}) > (3.5–3.8 wt%), which means that the fraction of the coarse phase will increase and is difficult to decrease even at high temperatures, and the quenching sensitivity will be intensified[4,5] (i.e., AA7136 alloy).

One can find that the second phases can be fully dissolved by one-step homogenization for the alloys with (Cu + Mg) content less than the critical value (4.16–4.20 wt% for Zn = 6.5–7.2 wt% or 3.5–3.8 wt% for Zn = 8.5–10.0 wt%), but the solute segregation in different alloys may be varied depending on whether excess Mg or Cu atoms appear, which also affects the homogenization process. It is known that the stoichiometric balance line model[75] can be used to determine the excess Cu or Mg content and help designing the homogenization process. Assuming that two precipitation reactions occur successively. All Zn atoms are consumed in forming the η phase including partial Mg atoms (η-$MgZn_2$, Mg wt%: Zn wt% = 24 × 1: 65 × 2 ≈ 0.19), and other Mg atoms are bounden with the S phase (S-Al_2CuMg, Mg wt%: Cu wt% = 24 × 1: 64 × 1 ≈ 0.37). Finally, a thermodynamic equilibrium state is approached without excess Mg or Cu atoms and the corresponding concentration equation can be expressed as a linear relationship between Cu and Mg contents at a constant Zn content: 0.19 C_{Zn} + 0.37 C_{Cu} = C_{Mg}. Small deviations from the model include: (1) some Cu atoms may be contained in the $MgZn_2$ structure; (2) a few Zn, Mg and Cu atoms are still in the aluminium matrix after aging; (3) the complete thermodynamic equilibrium cannot be approached. But these are not significant with respect to the overall conceptual model as to the stoichiometric balance between Zn, Mg and Cu atoms and will not affect the relationship therebetween and the model accuracy [75]. Then, the equilibrium isothermal phase diagram can be divided into three regions: the region near the stoichiometric balance line, excess Cu or Mg region, as shown in Fig. 14(a) and 15(b, c, d). Generally, for the alloys with (Cu + Mg) content less than the critical value and in the region near the stoichiometric balance line, especially on the stoichiometric balance line, the one-step homogenization treatment (≤475 °C for Zn = 6.5–7.2 wt% or ≤ 460 °C for Zn = 8.5–10.0 wt%) can be used. However, the solute segregation caused by excess Cu or Mg atoms needs higher temperatures or longer times to be uniformized for the alloys with (Cu + Mg) content less than the critical value but in the excess Cu or Mg region. The more the excess Cu or Mg atoms, the more serious the solute segregation, and the higher or longer the homogenization temperature or time needed. The above analysis reveals that the solubility limit and stoichiometric balance principles can be used to guide the homogenization process for Al-Zn-Mg-Cu alloys in order to control the homogenized microstructures as well as improving their comprehensive properties [46,56,76].

4.4. Confirming the principles with classical high-strength aluminium alloys

The effect of the residual coarse phases (i.e., the S or M/T phase) and precipitates (i.e., grain boundary and matrix precipitates) depending on the key alloying elements on the strength, corrosion resistance and fracture toughness are considered in this study. Previous study [77] indicated that the principle of optimizing the strength and toughness by maintaining the solute content at or just below the solid solubility limit transcends the different precipitation sequences and morphologies, and the present study considers the solubility limit along with stoichiometric balance with controlling the homogenized microstructures. It is known that

the fracture resistance or toughness of the Al-Zn-Mg-Cu alloys can be affected by the coarse intermetallic phases, dispersoids and grain structures as well as precipitates[78]. Especially, the coarse particles may cause microvoid nucleation via cracking or interfacial debonding, providing a preferred cracking path so as to decrease the crack propagation energy as well as the toughness [43,79], which might benefit from the key alloying elements level below the solubility limits for less or eliminating the coarse second phases[31,77,80,81] (i.e., the higher K_{IC} for the alloy in the α-Al single phase field than that in the two phase field as shown in the Fig. 16). Besides, the corrosion resistance may be also affected by the grain structures, intermetallics and precipitates. The effects of the first two factors are assumed to be similar for all present alloys, and the influences of the few Fe- or Si-enriched phases can be ignored compared to the above key factors. Furthermore, the quenching rate is very high (~100 °C/s) after solution treatment, which can inhibit the quench-induced precipitates [20,82]. The precipitation strengthening response as the dominant contribution to the strength of the Al-Zn-Mg-Cu alloy is greatly determined by the size, number density and volume fraction of the matrix precipitates (i.e., GP zone and η' phase), which mainly depends on the key alloying elements levels (i.e., Zn, Mg and Cu elements). Once the key alloying elements levels are beyond the solubility limit (i.e., within the two phase field in Fig. 14(a) or in the (α-Al + *M*/*T*) phase field in Fig. 16), the residual coarse phases (i.e., the *S* or *M*/*T* phase) may be formed and consume some of the Zn, Mg and Cu solutes [83-85], thus reducing the solute supersaturation and final aging hardening response [8,86] and causing localized failure as the preferential nucleation sites for microcracks [8,77]. When the key alloying elements levels are in the α-Al single phase field and near the solubility limit, these elements can be completely dissolved into the matrix during homogenization for a high solute supersaturation that will benefit the strength (i.e., the higher strength in the dark-blue box as shown in the Fig. 16). In addition, an overall saturation reduction of the composition with respect to the theoretical maximum solubility might benefit the low quenching sensitivity and the fracture toughness, i.e., the AA7040, AA7085 and AA7056 alloys [4,74,86], and the key alloying elements levels below the solubility limit also benefit the corrosion properties such as the stress corrosion cracking (SCC) resistance due to the absence of coarse residual phases[87] and related galvanic corrosion damages. For the Al-Zn-Mg-Cu alloys, the coarse residual phases (*M*/*T*/*S*) along grain boundaries (mostly) or in the matrix (few) may highly affect the corrosion resistance. On the one hand, they may act as a typical "variable polarity" phase to form the corrosion electrochemical microcell due to the active Mg/Zn atoms with the cathode matrix and the dealloying reaction [88,89], leading to the dissolution of active Mg/Zn atoms and the remaining Cu-enriched phase in the initial anode sites. As such, the electrochemical activity of the residual Cu-enriched phase is reduced and become noble relative to the surrounding active grain boundaries or the matrix, and this residual Cu-enriched phase can further act as the cathode together with the anodic grain boundaries and/or matrix to form the electrochemical microcell and promote the dissolution or pitting/intergranular corrosion [88,89]. The localized corrosion damages may be changed into the microcracks under stresses leading to SCC failure [90,91]. On the other hand, the corrosion properties are directly connected with the Cu content of grain boundary precipitates[92] and can be improved by increasing it due to the reduced potential difference between the grain boundary and the matrix or precipitate-free zones (PFZs). Previous study[92] indicated that the residual coarse phase (such as the *S* phase) decreased the Cu concentration in the matrix and subsequently the Cu concentration in the grain boundary precipitates, thus increasing the anodic reaction kinetic of the grain boundary precipitates and accelerating the dissolution of the grain boundary precipitates, and finally the SCC threshold value (K_{ISCC}) was decreased. However, even though the key alloying elements levels are below the solubility limit, excess Mg or Cu atoms and/or the stoichiometric balance may also appear[75], for which the excess Mg may segregate towards grain boundaries and decrease the SCC resistances via grain boundary anodic dissolution and/or Mg-H complex-induced cracking[14,86,93-100] (i.e., the high K_{IC} and good SCC resistance in the Mg excess region in Fig. 16). For the excess-Cu alloys, less coarse phases may be along grain boundaries and the fracture toughness will be slightly affected compared to that of the excess-Mg alloys[101]. Furthermore, higher Cu concentration of the grain boundary precipitates is beneficial for SCC resistance[10], and thus the excess-Cu alloy may exhibit better fracture toughness and SCC resistance than that of the excess-Mg alloys[75,101] (as shown in the Fig. 16). As a result, the excess Cu may exhibit less adverse effect to the comprehensive properties compared with that of excess Mg and the stoichiometric balance among Zn, Mg and Cu elements can promote complete/efficient precipitation during aging and avoid excess Mg or significantly excess Cu atoms, i.e., the dark-yellow box area with a stoichiometric balance among Zn, Mg and Cu elements more preferably or slightly Cu excess in Fig. 16 shows the highest K_{IC} and best SCC resistance.

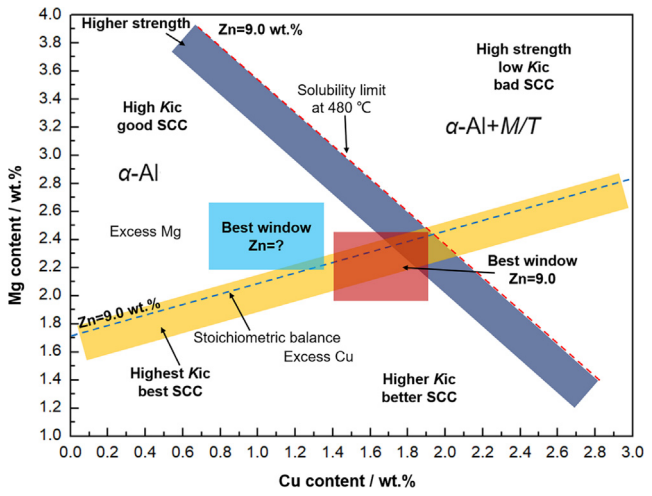

Fig. 16. The designed best composition windows of the alloy with 9.0 wt%Zn based on the homogenized microstructure and the solubility limit and stoichiometric balance principles.

The above analysis reveals that the solubility limit and stoichiometric balance principles based on the control of the homogenized microstructures can be used for alloying design reexamination, thus its accuracy/reliability is verified by analyzing the correlation between the composition and comprehensive properties of typical Al-Zn-Mg-Cu alloys. It's noteworthy that for the alloys with Zn <=8.0 wt%, the solubility limits are estimated by the solvus of the *S* phase at 490 °C due to the residual *S* phase transformed from the *M* and/or *T* phase[49,55], while for the alloys with Zn > 8.0 wt %, the solubility limits are estimated by the solvus of the *M* and/or *T* phase at ~480 °C because no *S* phase is remained[49,55]. As shown in Fig. 17(a), according to solubility limit and stoichiometric balance principles, it can be estimated that the strengths of AA7050, AA7010 and AA7040 alloys are relatively similar but the latter two has higher fracture toughness. Obviously, the latter two alloys are in α-Al single-phase field while AA7050 alloy is in α-Al single phase field and/or (α-Al + *S*) phase field, which means a possible residue of the *S* phase after the homogenization or solid solution treatment that is detrimental to the fracture toughness[31,74]. Moreover, the alloying levels of AA7040 and AA7050 alloys are clo-

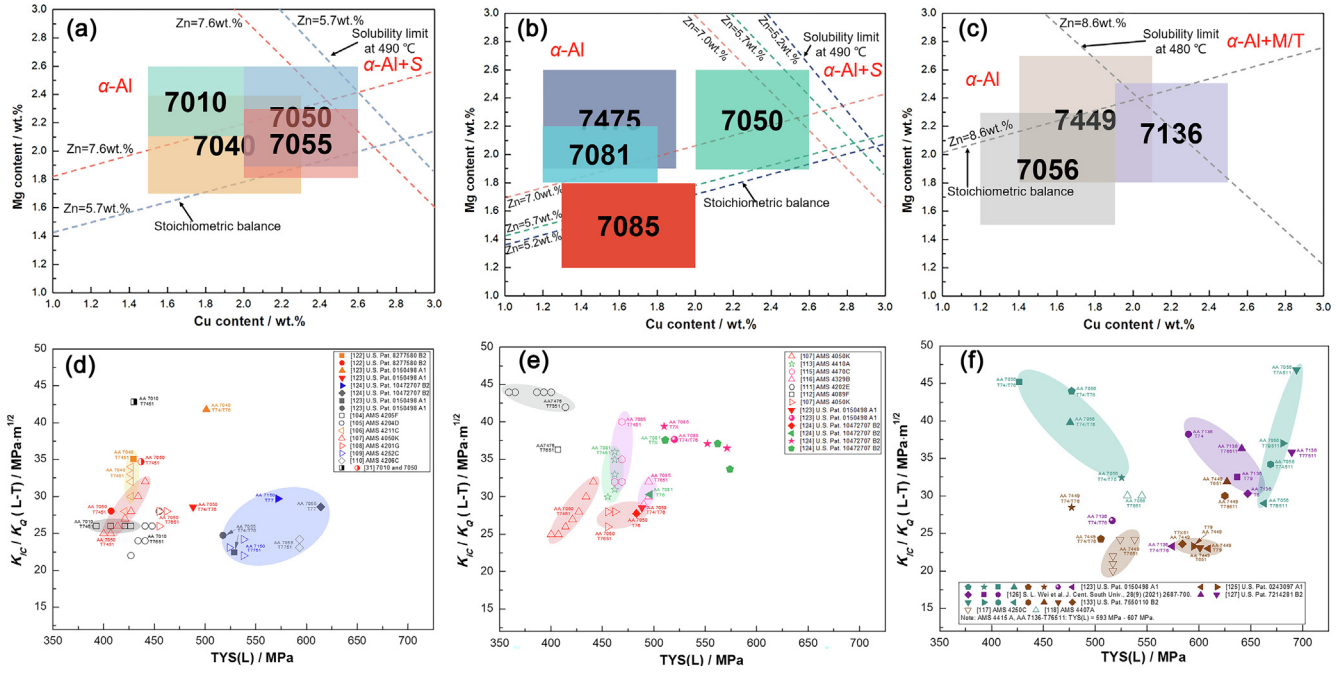

Fig. 17. The estimation of the comprehensive properties of the typical alloys based on the solubility limit and stoichiometric balance principles: (a) AA7050, AA7010, AA7040 and AA7055; (b) AA7081, AA7085, AA7475 and AA7050; (c) AA7056, AA7136 and AA7449; and the actual strength and toughness performance from AMS standards and patents, etc: (d) AA7050, AA7010, AA7040 and AA7055; (e) AA7081, AA7085, AA7475 and AA7050; (f) AA7056, AA7136 and AA7449.

ser to or on the stoichiometric balance line but it is far away from the stoichiometric balance line for AA7010 alloy, which would be in excess-Mg region that may cause inferior SCC resistance [14,86,100]. Furthermore, the fracture toughness and SCC resistance of AA7055 alloy are higher or better than that of AA7150 (close to AA7050) alloy (Fig. 17(a)). Similarly, the strength and fracture toughness of AA7081 alloy are higher than that of AA7050 alloy (Fig. 17(b)) while their SCC resistance is comparable due to the similar Mg excess levels. For AA7475 and AA7085 alloys (Fig. 17(b)), the strength and SCC resistance of the latter is better than that of the former but with similar fracture toughness. Both AA7085 and AA7081 alloys (Fig. 17(b)) exhibit similar strength and fracture toughness but the former has better SCC resistance due to its Cu excess. In addition, based on the relationship between the solubility limit line at 480 °C or the stoichiometric balance line and the alloy composition range, the AA7136 alloy may exhibit the highest strength but with the lowest fracture toughness and SCC resistance among the three alloys in Fig. 17(c). The above estimated comprehensive properties of typical alloys based on the solubility limit and stoichiometric balance principles agree well with the actual measurements[4,6,31,49,74,85,101-127], as shown in Fig. 17(d, e, f), showing good reliability.

Thus, there is a correlation among the composition, homogenization microstructures and properties, and based on the homogenized microstructures, the alloy compositions with specific microstructures (under the optimal heat treatment process) and excellent comprehensive properties can be designed/optimized according to the solubility limit and stoichiometric balance principles. For example, the composition windows (red box in Fig. 16) for Zn = 9.0 wt% could contribute to a good integrated property. The established alloying design approach can be further proved to be reliable based on previous studies (Fig. 18)[101,102,128-133]. Specifically, the composition of Al-7.12Zn-2.02 Mg-2.13Cu with well-balanced strength and toughness (Fig. 18(a))[128] is within the brown-dotted box (Fig. 18(b)) but with slight Cu excess. However, the slight Mg excess occurs in Al-7.02Zn-2.14 Mg-1.89Cu alloy, thereby deteriorating the toughness and corrosion performance although it can raise the strength. In addition, the Al-8.1Zn-1.92 Mg-1.94Cu alloy with well-balanced strength and toughness (Fig. 18(a))[129] is within the purple-dotted box (Fig. 18(b)) and with slight Cu excess, which is anticipated to be conducive to improve the SCC resistance based on the stoichiometric balance principle. In contrast, other alloys in Fig. 18(b) with either lower Cu and/or Mg content or higher Cu and/or Mg content exhibit low strength and high toughness or high strength and low toughness, respectively (Fig. 18(a)). As shown in Fig. 18(b), the designed composition range within the gray-dotted box according to the present approach has been proved with better comprehensive properties previously[101], i.e., with increasing the Mg or Cu content, the strength increases and toughness decreases, and the effect of the Mg content on the strength and toughness is more significant (Fig. 18(a)). Therefore, the alloys with the mediate/high Mg content (~2.0 - ~2.5 wt%) and low/mediate Cu content (~1.5 - ~2.0 wt%) are preferable for better comprehensive properties although small composition deviation may appear practically.

A recently designed high-strength Al alloy (Al - (8.3–9.5)Zn - (2.0–2.5)Mg - (1. 3-1.8)Cu, wt%) with good combination of strength and toughness[102,130,131] (Fig. 18(a)) is well consistent with the composition window (blue-dotted box in Fig. 18(b)) obtained with above principles. For example, the fracture toughness of the Al-8.90Zn-2.29 Mg-1.76Cu alloy (wt%, 33.2 MPa·m$^{1/2}$) are comparable to that of the AA7050 and AA7136 alloys (~33 MPa·m$^{1/2}$)[107,127] but with higher tensile strength (>720 MPa) (Fig. 18(a)). The optimal alloy compositions (orange (Al - (8.55–8.66)Zn - (2. 3-2.33)Mg - (1.74–1.84)Cu, wt%) or green (Al - (8.96–9.23)Zn - (2.26–2.28)Mg - (1.83-1.92)Cu, wt%) points) with excellent tensile strength and toughness combination (730 MPa and 34 MPa·m$^{1/2}$, or 750 MPa and 33 MPa·m$^{1/2}$)[102] are within the gray- (~8.5 wt% Zn) and blue-dotted (~9.0 wt% Zn) composition window in Fig. 18(b), respectively. Besides, the composition of Al-9.3Zn-2.4 Mg-(1.5, 1.8)Cu[132] with better balance of tensile strength and toughness (Fig. 18(a)) is within the red-dotted composition window in Fig. 18 (b), while other alloys with the composition of Al-9.3Zn-2.4 Mg-(0.8, 1.3 or 2.2)Cu exhibit higher strength and low toughness or

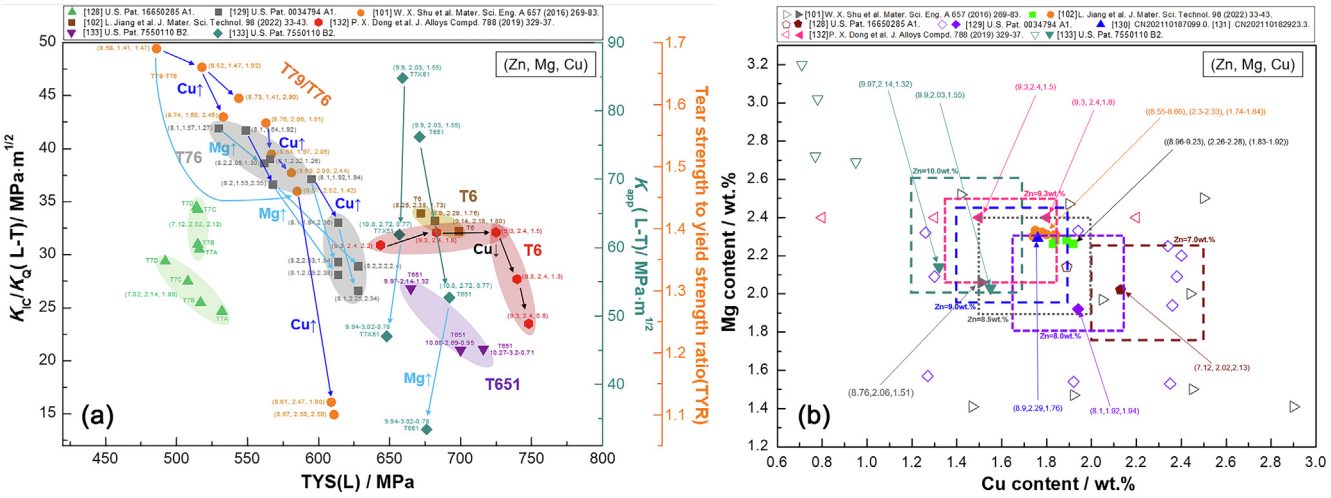

Fig. 18. The validation of the established alloying approach based on the previous studies[101,102,128-133] (wt%): (a) the strength and toughness properties of the studied alloys, Al-(~7.0)Zn-yMg-xCu alloys[128], Al-(~8.0)Zn-yMg-xCu alloys[129], Al-8.5 Zn-(1.5 ~ 2.5)Mg-(1.5 ~ 3.0)Cu alloys[101], Al-(8.3 ~ 9.5)Zn-(1.9 ~ 2.5)Mg-(1.4 ~ 2.0)Cu alloys[102,130,131], Al-9.3Zn-2.4 Mg-(0.8 ~ 2.2)Cu alloys[132], Al-10.0Zn-yMg-xCu alloys[133]; and (b) the designed best composition windows of the Al-Zn-Mg-Cu alloys with a certain Zn content.

lower strength and lower toughness, respectively, all of which are the results from the competitions between the residual coarse phase fractions and the contrast of yield stress in the matrix and grain boundary zones under the effect of the Cu content. In addition, the size of the plastic zones decreases with the increase of strength for the alloy with the low Cu content, which may also decrease the fracture toughness. Furthermore, based on the above approach, the higher-Zn alloys (10 wt%) with good integrated properties may be located within the dark-green-dotted composition window in Fig. 18(b) and two alloys with composition of Al-9.97Zn-2.14 Mg-1.32Cu and Al-9.90Zn-2.03 Mg-1.55Cu[133] were confirmed with better balance of tensile strength and toughness (Fig. 18(a)). While other alloys with high Mg: Cu ratios (i.e., Al-10.27Zn-3.2 Mg-0.71Cu or Al-10.0Zn-2.72 Mg-0.77Cu) exhibit lower fracture toughness along with a comparable or lower strength level[133].

The solubility limit and stoichiometric balance principles based on controlling the homogenized microstructures can be used to design or optimize the compositions of advanced high-strength Al-Zn-Mg-Cu alloys and related high-temperature treatments (i.e., homogenization and solution treatments). From the above thermodynamic approach, the preferable composition windows at a certain Zn content (such as 7.2 wt%), as shown in the Fig. 19, will exhibit balanced strength, toughness and SCC resistance. In a word, the present approach can greatly shorten and/or reduce the time and/or costs of alloy composition design compared with the traditional design method based on the final performance evaluation.

5. Conclusions

The as-cast and homogenized microstructures of a series of high-strength Al-Zn-Mg-Cu alloys were studied along with thermodynamic calculation for clarifying the mutual relationship among the composition, microstructure and homogenization process. The main conclusions are as follows.

(1) The as-cast alloys mainly contain the eutectic *M* phase and Cu-enriched [AlCuMgZn] phase except for the alloys with (Cu + Mg) ~< 4.08 wt%, along with minor θ (Al_2Cu) and Al_7Cu_2Fe phases. The fraction of the *M* phase can be maximized with critical Zn:Mg ratio and lower (Cu + Mg) content, while the Cu-enriched or *S* phase can be avoided with Zn:Mg ~>3.41 and/or (Cu + Mg) ~<4.08 wt%.

(2) The *M* phase (and the Cu-enriched [AlCuMgZn] phase) and the *S* phase transformed from the partial *M* and Cu-enriched [AlCuMgZn] phases can be completely dissolved after the homogenization for the low-(Cu + Mg) (i.e., alloys 1-1, 2-1, 3-1 and 3-2) and the mediate-(Cu + Mg) alloys (i.e., alloy 2-2), while the residual *S* phase appears in the high-(Cu + Mg) alloys (i.e., alloys 1-2 and 3-3). In total, the homogenization process is directly related to the formation of the *S* phase that firstly depends on the (Cu + Mg) content and secondarily on the Zn:Mg ratio, and the alloys with (Cu + Mg) content > 4.24 wt% cannot be fully homogenized even with the two-step homogenization process (475 °C/24 h + 485 °C/24 h) because of the residual *S* phase.

(3) The kinetic analysis indicates that the dissolution of intragranular phases and uniform solute distribution can be achieved after 475 °C/~5h homogenization, while the dissolution of intergranular phase and solute distribution can be

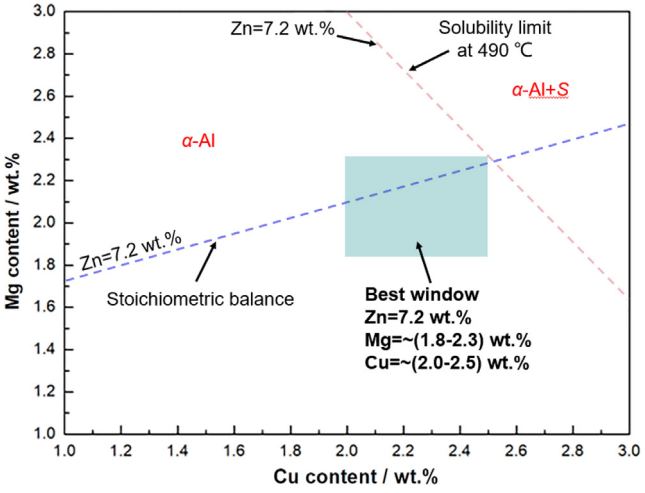

Fig. 19. The best composition windows for the studied alloys with a certain Zn content(7.2 wt%).

achieved after 475 °C/ (4–32) h homogenization, which is in line with the experiments except for the insoluble grain boundary phases.

(4) Both the solubility limit and stoichiometric balance principles can be applied to determine the critical (Cu + Mg) value and the linear correlation between Cu and Mg contents and to design or optimize the composition and homogenization process for Al-Zn-Mg-Cu alloys. This could pave an efficient way for designing advanced high-strength Al alloys or other heat-treatable metallic alloys compared to traditional method based on final performance evaluation.

CRediT authorship contribution statement

Y. W. Wang: Methodology, Formal analysis, Investigation, Writing - original draft. **L. G. Hou:** Conceptualization, Formal analysis, Project administration, Funding acquisition, Resources, Writing - review & editing. **H. Su:** Methodology, Resources. **Q. K. Tian:** Methodology, Resources. **K. C. Yu:** Methodology, Resources. **D. G. Eskin:** Writing - review & editing. **L. Katgerman:** Writing - review & editing. **L. Z. Zhuang:** Supervision, Funding acquisition, Project administration, Writing - review & editing.

Declaration of Competing Interest

The authors declare that they have no known competing financial interests or personal relationships that could have appeared to influence the work reported in this paper.

Acknowledgements

The authors would like to acknowledge the financial support from the Constructed Project for Key Laboratory of Beijing, China [No. BJSJ2019004], the State Key Laboratory for Advanced Metals and Materials of China [No. 2018Z-23], and the International S&T Cooperation Projects of Nanjing, China [No. 201818014].

Data Availability statement

The raw/processed data required to reproduce these findings cannot be shared at this time as the data also form part of an ongoing study.

Appendix A. Supplementary data

Supplementary data to this article can be found online at https://doi.org/10.1016/j.matdes.2022.110975.

References

[1] Aluminum Association, International alloy designations and chemical composition limits for wrought aluminum and wrought aluminum alloy[S]. The Aluminum Association, 2015.
[2] I. Polmear, D. StJohn, J. F. Nie, M. Qian, Light alloys: Wrought Aluminium Alloys (Fifth Edition), Butterworth-Heinemann, 2017, pp. 157-263.
[3] J.C. Williams, E.A. Starke, Progress in structural materials for aerospace systems, Acta Mater. 51 (19) (2003) 5775–5799.
[4] J. Boselli, G. Bray, R. J. Rioja, D. Mooy, G. Venema, G. Feyen, W. Wang, The metallurgy of high fracture toughness aluminum-based plate products for aircraft internal structure, ICAA13. Pittsburgh, (2012) 581-6.
[5] J. Boselli, D.J. Chakrabarti, R.T. Shuey, Aerospace applications: metallurgical insights into the improved performance of aluminum alloy 7085 thick products, Al Alloys 1 (2008) 202–208.
[6] D.J. Chakrabarti, J. Liu, R.R. Sawtell, G.B. Venema, New generation high strength high damage tolerance 7085 thick alloy product with low quench sensitivity, Mater. Forum. 28 (2004) 969–974.
[7] M. Dixit, R.S. Mishra, K.K. Sankaran, Structure-property correlations in Al 7050 and Al 7055 high-strength aluminum alloys, Mater. Sci. Eng. A 478 (1–2) (2008) 163–172.
[8] J. T. Staley, "Microstructure and toughness of high-strength aluminum alloys," Properties related to fracture toughness, ASTM STP 605, Am. Soc. Test. Mater. (1976) 71-103.
[9] D. Dumont, A. Deschamps, Y. Brechet, On the relationship between microstructure, strength and toughness in AA7050 aluminum alloy, Mater. Sci. Eng. A 356 (1–2) (2003) 326–336.
[10] A. Garner, R. Euesden, Y.C. Yao, Y. Aboura, H. Zhao, J. Donoghue, M. Curioni, B. Gault, P. Shanthraj, Z. Barrett, C. Engel, T.L. Burnett, P.B. Prangnell, Multiscale analysis of grain boundary microstructure in high strength 7xxx Al alloys, Acta Mater. 202 (2021) 190–210.
[11] B. Zhou, B. Liu, S.G. Zhang, The advancement of 7xxx series aluminum alloys for aircraft structures: A review, Metals 11 (5) (2021) 718.
[12] H. Su, S. Bhuiyan, H. Toda, K. Uesugi, A. Takeuchi, Y. Watanabe, Influence of intermetallic particles on the initiation and growth behavior of hydrogen micropores during high-temperature exposure in Al-Zn-Mg-Cu aluminum alloys, Scr. Mater. 135 (2017) 19–23.
[13] S.T. Lim, Y.Y. Lee, I.S. Eun, Dilute alloy designs of 7xxx aluminum alloys for thick forging applications, Mater. Sci. Forum 475 (2005) 369–372.
[14] S.T. Lim, I.S. Eun, S.W. Nam, Control of equilibrium phases (*M*, *T*, *S*) in the modified aluminum alloy 7175 for thick forging applications, Mater. Trans. 44 (1) (2003) 181–187.
[15] F.Y. Xie, X.Y. Yan, L. Ding, F. Zhang, S.L. Chen, M.G. Chu, Y.A. Chang, A study of microstructure and microsegregation of aluminum 7050 alloy, Mater. Sci. Eng. A 355 (1–2) (2003) 144–153.
[16] Y.H. Zhou, Z.Q. Hu, W.Q. Jie, Solidification Technology, Machinery Industry Press, Beijing, 1998, p. 13.
[17] Y. Zou, X.D. Wu, S.B. Tang, Q.Q. Zhu, H. Song, M.X. Guo, L.F. Cao, Investigation on microstructure and mechanical properties of Al-Zn-Mg-Cu alloys with various Zn/Mg ratios, J. Mater. Sci. Technol. 85 (2021) 106–117.
[18] S.J. Won, H. So, L. Kang, S.J. Oh, K.H. Kim, Development of a high-strength Al-Zn-Mg-Cu-based alloy via multi-strengthening mechanisms, Scr. Mater. 205 (2021) 114216.
[19] C. Mondal, A.K. Mukhopadhyay, On the nature of *T* ($Al_2Mg_3Zn_3$) and *S* phases present in as-cast and annealed 7055 aluminum alloy, Mater. Sci. Eng. A 391 (1–2) (2005) 367–376.
[20] G. Graf, P. Spoerk-Erdely, P. Staron, A. Stark, F.M. Martin, H. Clemens, T. Klein, Quench rate sensitivity of age-hardenable Al-Zn-Mg-Cu alloys with respect to the Zn/Mg ratio: an in situ SAXS and HEXRD study, Acta Mater. 227 (2022) 117727.
[21] D. Xu, Z.H. Li, G.J. Wang, X.W. Li, X.Y. Lv, Y.A. Zhang, Y.Q. Fan, B.Q. Xiong, Phase transformation and microstructure evolution of an ultra-high strength Al-Zn-Mg-Cu alloy during homogenization, Mater. Charact. 131 (2017) 285–297.
[22] M. Ajay Krishnan, V. S. Raja, Mitigating environmentally assisted cracking in 7xxx Cu containing aluminum alloys, A Treatise on Corrosion Science, Engineering and Technology. Springer, Singapore, 2022, pp. 223-36.
[23] Z.G. Chen, Z.G. Yuan, J.K. Ren, The mechanism of comprehensive properties enhancement in Al-Zn-Mg-Cu alloy via novel thermomechanical treatment, J. Alloys Compd. 828 (2020) 154446.
[24] Y. Zou, L.F. Cao, X.D. Wu, Y.C. Wang, X. Sun, H. Song, M.J. Couper, Effect of ageing temperature on microstructure, mechanical property and corrosion behavior of aluminum alloy 7085, J. Alloys Compd. 823 (2020) 153792.
[25] S.L. Wei, R.C. Wang, H. Zhang, C.H. Xu, Y. Wu, Y. Feng, Influence of Cu/Mg ratio on microstructure and mechanical properties of Al-Zn-Mg-Cu alloys, J. Mater. Sci. 56 (4) (2021) 3472–3487.
[26] C.L. Liu, A. Davis, J. Fellowes, P.B. Prangnell, D. Raabe, P. Shanthraj, CALPHAD-informed phase-field model for two-sublattice phases based on chemical potentials: η-phase precipitation in Al-Zn-Mg-Cu alloys, Acta Mater. 226 (2022) 117602.
[27] Z.P. Wang, M.L. Wang, Y.G. Li, H.Y. Xiao, H. Chen, J.W. Geng, X.F. Li, D. Chen, H. W. Wang, Effect of pretreatment on microstructural stability and mechanical property in a spray formed Al-Zn-Mg-Cu alloy, Mater. Des. 203 (2021) 109618.
[28] J.A. Österreicher, M.A. Tunes, F. Grabner, A. Arnoldt, T. Kremmer, S. Pogatscher, C.M. Schlögl, Warm-forming of pre-aged Al-Zn-Mg-Cu alloy sheet, Mater. Des. 193 (2020) 108837.
[29] K.Y. Xiang, X.C. Lei, L.P. Ding, Z.H. Jia, X.F. Yang, Q. Liu, Optimizing mechanical property of spray formed Al-Zn-Mg-Cu alloy by combination of homogenization and warm-rolling, Mater. Sci. Eng. A 846 (2022) 143248.
[30] J. Luo, H.Y. Luo, S.J. Li, R.Z. Wang, Y. Ma, Effect of pre-ageing treatment on second nucleating of GPII zones and precipitation kinetics in an ultrafine grained 7075 aluminum alloy, Mater. Des. 187 (2020) 108402.
[31] A.J. Morris, R.F. Robey, P.D. Couch, E., De los Rios, A comparison of the damage tolerance of 7010 T7451 and 7050 T7451, Mater. Sci. Forum 242 (1997) 181–186.
[32] T. R. Prabhu, An overview of high-performance aircraft structural Al alloy-AA7085, Acta Metall. Sin. (Engl. Lett.) 28 (7) (2015) 909-21.
[33] Y.X. Li, P. Li, G. Zhao, X.T. Liu, J.Z. Cui, The constituents in Al-10Zn-2.5Mg-2.5Cu aluminum alloy, Mater. Sci. Eng. A 397 (1–2) (2005) 204–208.
[34] R. Ghanghas, C. Mondal, D. Kumar, P. Ghosal, In-situ dissolution behavior of secondary alloy phases in Al–Zn–Mg–Cu-base AA7055 aluminum alloy, Applications of Microscopy in Materials and Life Sciences. Springer, Singapore, 2021, pp. 145-57.
[35] W. Wang, R. T. Shuey, Homogenization model for 7xxx aluminum alloys. In: Proceedings of the ICAA12. Yokohama, (2010) 264-9.
[36] Y.W. Shao, Y. Liu, J.F. Leng, K. Zhu, Z.M. Liu, C.X. Li, Microstructure of as-cast 7085 aluminum alloy by homogenization, Mater. Sci. Forum 898 (1) (2017) 265–271.

[37] T. Sheppard, Extrusion of aluminium alloys, Springer Science and Business Media, 1999.
[38] J.T. Liu, Y.A. Zhang, X.W. Li, Z.H. Li, B.Q. Xiong, J.S. Zhang, Thermodynamic calculation of Al-9.5Zn-2.0Mg-1.7Cu alloy, J. Aeronaut. Mater. 33 (6) (2013) 1–7.
[39] J.J. Yu, X.M. Li, X.Q. Yu, Thermodynamic analyse on equilibrium precipitation phases and composition design of Al-Zn-Mg-Cu alloys, J. Shanghai Jiaotong Univ. (Sci.) 17 (3) (2012) 286–290.
[40] J.T. Liu, Y.A. Zhang, X.W. Li, Z.H. Li, B.Q. Xiong, J.S. Zhang, Thermodynamic calculation of high zinc-containing Al-Zn-Mg-Cu alloy, Trans. Nonferrous Met. Soc. China 24 (5) (2014) 1481–1487.
[41] J. Wang, Y.A. Zhang, Y.Q. Fan, L.B. Jin, X.W. Li, Z.H. Li, Microstructure of semicontinuous casting ingot and homogenization of high Zn-containing Al-Zn-Mg-Cu Alloys with Zn and Mg additives, Rare Met. 11 (2016) 1081–1087.
[42] Y.L. Deng, Z.M. Yin, F.G. Cong, Intermetallic phase evolution of 7050 aluminum alloy during homogenization, Intermetallics 26 (2012) 114–121.
[43] W.X. Shu, L.G. Hou, J.C. Liu, C. Zhang, F. Zhang, J.T. Liu, L.Z. Zhuang, J.S. Zhang, Solidification paths and phase components at high temperatures of high-Zn Al-Zn-Mg-Cu alloys with different Mg and Cu contents, Metall. Mater. Trans. A 46 (2015) 5375–5392.
[44] B.H. Nie, P.Y. Liu, T.T. Zhou, Effect of compositions on the quenching sensitivity of 7050 and 7085 alloys, Mater. Sci. Eng. A 667 (2016) 106–114.
[45] W.X. Shu, J.C. Liu, L.G. Hou, H. Cui, J.T. Liu, J.S. Zhang, Microstructural evolution of Al-8.59Zn-2.00Mg-2.44Cu during homogenization, Int. J. Miner., Metall. Mater. 21 (12) (2014) 1215–1221.
[46] G.S. Wang, Q.Q. Chen, K. Tao, Q.C. Chen, Z.H. Zhao, Effect of homogenizing treatment on microstructure and property of Al-Zn-Mg-Cu-Zr aluminum alloy, Mater. Sci. Forum 877 (2016) 587–592.
[47] H. Chen, S.X. Gao, P.A. Rometsch, D.K. Xu, B.C. Muddle, Dissolution and melting of constituent particles in a DC-cast Al-Zn-Mg-Cu alloy 7150 during homogenization, in: In: The Japan Inst Light Met. Proceedings of the 12th International Conference on Aluminum Alloys, 2010, pp. 1656–1661.
[48] Z.H. Li, Y.A. Zhang, B.Q. Xiong, Y.Q. Fan, X.W. Li, H.W. Liu, F. Wang, R. r., in: Zhu, Investigation on microstructure in as-cast aluminum alloy 7136 and its evolution during homogenization, Springer, Cham, 2013, pp. 1299–1305.
[49] K. Wen, B.Q. Xiong, Y.A. Zhang, G.J. Wang, X.W. Li, Z.H. Li, S.H. Huang, H.W. Liu, Microstructure evolution of a high Zinc containing Al-Zn-Mg-Cu alloy during homogenization, Rare Met. Mater. Eng. 46 (4) (2017) 928–934.
[50] F.L. Zhai, L.P. Wang, X. Gao, Y.C. Feng, S.C. Zhao, L. Wang, Phase evolution of a novel Al–Zn–Mg–Cu–Zr–Sm alloy during homogenization annealing treatment, Mater. Res. Express 7 (7) (2020) 076518.
[51] X.M. Qian, X.L. Li, Y. Li, G.M. Xu, Z.D. Wang, Microstructure evolution during homogenization and hot workability of 7055 aluminum alloy produced by twin-roll casting, J. Mater. Res. Technol. 13 (2021) 2536–2550.
[52] F.Y. Xie, T. Kraft, Y. Zuo, C.H. Moon, Y.A. Chang, Microstructure and microsegregation in Al-rich Al-Cu-Mg alloys, Acta Mater. 47 (2) (1999) 489–500.
[53] S.T. Lim, Y.Y. Lee, I.S. Eun, Microstructural evolution during ingot preheat in 7xxx aluminium alloys for thick semiproduct applications, Mater. Sci. Forum 519 (2006) 549–554.
[54] X.G. Fan, D.M. Jiang, Q.C. Meng, B.Y. Zhang, T. Wang, Evolution of eutectic structures in Al-Zn-Mg-Cu alloys during heat treatment, Trans. Nonferrous Met. Soc. China 16 (3) (2006) 577–581.
[55] Y. Liu, D.M. Jiang, W.L. Xie, J. Hu, B.R. Ma, Solidification phases and their evolution during homogenization of a DC cast Al-8.35Zn-2.5Mg-2.25Cu alloy, Mater. Charact. 93 (2014) 173–183.
[56] P.F. Jia, Y.H. Cao, Y.D. Geng, L.Z. He, N. Xiao, J.Z. Cui, Studies on the microstructures and properties in phase transformation of homogenized 7050 alloy, Mater. Sci. Eng. A 612 (26) (2014) 335–342.
[57] X.Y. Lv, E.J. Guo, Z.H. Li, G.J. Wang, Research on microstructure in as-cast 7A55 aluminum alloy and its evolution during homogenization, Rare Met. 30 (6) (2011) 664–668.
[58] P.N. Adler, R. Deiasi, Calorimetric studies of 7000 series aluminum alloys: II. comparison of 7075, 7050 and RX720 alloys, Metall. Mater. Trans. A 8 (7) (1977) 1177–1183.
[59] X.G. Fan, D.M. Jiang, Q.C. Meng, L. Zhong, The microstructural evolution of an Al-Zn-Mg-Cu alloy during homogenization, Mater. Lett. 60 (12) (2006) 1475–1479.
[60] X.M. Li, M.J. Starink, Effect of compositional variations on characteristics of coarse intermetallic particles in overaged 7000 aluminium alloys, Mater. Sci. Technol. 17 (11) (2001) 1324–1328.
[61] H.J. Wang, J. Xu, Y.L. Kang, M.O. Tang, Z.F. Zhang, Study on inhomogeneous characteristics and optimize homogenization treatment parameter for large size DC ingots of Al-Zn-Mg-Cu alloys, J. Alloys Compd. 585 (2014) 19–24.
[62] X.M. Li, J.J. Yu, Modeling the effects of Cu variations on the precipitated phases and properties of Al-Zn-Mg-Cu Alloys, J. Mater. Eng. Perform. 22 (2013) 2970–2981.
[63] L. Wan, Y.L. Deng, Y.Y. Zhang, X.M. Zhang, Al-(7.8∼9.0)Zn-1.6Mg-(1.0∼2.2)Cu alloy as-cast and homogenization microstructures, Chin. J. of Nonferrous Met. 20 (9) (2010) 1698–1704.
[64] Y.J. Shi, Q.L. Pan, M.J. Li, Z.M. Liu, Z.Q. Huang, Microstructural evolution during homogenization of DC cast 7085 aluminum alloy, Trans. Nonferrous Met. Soc. China 25 (11) (2015) 3560–3568.
[65] D.L. Yuan, S.Y. Chen, L. Zhou, J.Y. Chang, K.H. Chen, As-cast and homogenized microstructure of Al-Zn-Mg-Cu alloy with high Zn and super strength, Chin. J. of Nonferrous Met. 28 (12) (2018) 2393–2403.
[66] P.F. Jia, Y.H. Cao, Y.D. Geng, L.Z. He, N. Xiao, J.Z. Cui, Studies on the microstructures and properties in phase transformation of homogenized 7050 alloy, Mater. Sci. Eng. A 612 (2014) 335–342.
[67] Q. H. Li, Influence of Zn:Mg ratio on mechanical properties of Al-Zn-Mg and Al-Zn-Mg-Cu aluminum alloys, Light Met. 03 (1980) 36-43, 54.
[68] P. Priya, D.R. Johnson, M. Krane, Modeling phase transformation kinetics during homogenization of aluminum alloy 7050, Comput. Mater. Sci. 138 (2017) 277–287.
[69] S.L. Yang, J. Shen, X.D. Yan, X.W. Li, F. Zhang, B.Q. Sun, Homogenization treatment parameter optimization and microstructural evolution of Al-Cu-Li alloy, Rare Met. Mater. Eng. 46 (1) (2017) 28–34.
[70] Y.J. Guo, J.F. Li, D.D. Lu, S.X. Deng, G.J. Zeng, Y.L. Ma, W. You, Y.L. Chen, X.H. Zhang, R.F. Zhang, Characterization of Al_3Zr precipitation via double-step homogenization and recrystallization behavior after subsequent deformation in 2195 Al-Li alloy, Mater. Charact. 182 (2021) 111549.
[71] Y.X. Wang, X.W. Ma, G.Q. Zhao, X. Xu, X.X. Chen, C.S. Zhang, Microstructure evolution of spray deposited and as-cast 2195 Al-Li alloys during homogenization, J. Mater. Sci. Technol. 82 (2021) 161–178.
[72] A.T. Little, W. Hume-Rothery, G.V. Raynor, The constitution of Al-Cu-Mg alloys at 460 °C, J. Inst. Met. 70 (1944) 491–506.
[73] D.J. Strawbridge, W. Hume-Rothery, A.T. Little, The constitution of Al-Cu-Mg-Zn alloys at 460 °C, J. Inst. Met. 74 (7) (1948) 191–225.
[74] R. Shahani, T. Warner, C. Sigli, P. Lassince, P. Lequeu, High strength 7xxx alloys for ultra-thick aerospace plate: optimisation of alloy composition, in: Aluminum Alloys: their physical and mechanical properties (ICAA6), 1998, pp. 1105–1110.
[75] K.R. Anderson, Method of producing an aluminum-zinc-magnesium-copper alloy having improved exfoliation resistance and fracture toughness, U.S. Pat. 5312498 (1994) May. 17.
[76] T. Xiao, Y.L. Deng, L.Y. Ye, H.Q. Lin, C.J. Shan, P.W. Qian, Effect of three-stage homogenization on mechanical properties and stress corrosion cracking of Al-Zn-Mg-Zr alloys, Mater. Sci. Eng. A 675 (2016) 280–288.
[77] W.A. Cassada, M.F. Bartholomeusz, The effect of Cu and Mg content on mechanical properties of Al-Cu-Mg alloys with and without Ag additions, Mater. Sci. Forum 217 (1996) 1765–1770.
[78] S.T. Lim, S.J. Yun, S.W. Nam, Improved quench sensitivity in modified aluminum alloy 7175 for thick forging applications, Mater. Sci. Eng. A 371 (1–2) (2004) 82–90.
[79] W.X. Shu, Solidification characteristics and strengthening-toughening mechanisms of 7xxx Al alloys with tailored Mg and Cu elements, University of Science and Technology Beijing, Beijing, 2016. Doctoral dissertation.
[80] P. Sainfort, C. Sigli, G.M. Raynaud, P. Gomiero, Structure and property control of aerospace alloys, Mater. Sci. Forum 242 (1997) 25–32.
[81] D.S. Thompson, Metallurgical factors affecting high strength aluminum alloy production, Metall. Mater. Trans. A 6 (4) (1975) 671–683.
[82] L.H. Lin, H.J. Peng, J.G. Zhao, Quench sensitivity of 7475 aluminum alloy using end-quenching technique and TTP diagrams, JOM 73 (4) (2021) 1135–1143.
[83] K.K. Sankaran, R.S. Mishra, Metallurgy and design of alloys with hierarchical microstructures, Elsevier, 2017.
[84] M. Tiryakioğlu, J.T. Staley, Physical metallurgy and the effect of alloying additions in aluminum alloys, Handbook of aluminum 1 (2003) 81–210.
[85] J.E. Starke, Alloying of aluminum: Development of new aluminum alloys, Alloying, ASM International, 1988, pp. 165–197.
[86] T. Warner, Recently-developed aluminium solutions for aerospace applications, Mater. Sci. Forum 519 (2006) 1271–1278.
[87] A.K. Mukhopadhyay, Selection and design principles of wrought aluminium alloys for structural applications, Mater. Sci. Forum 710 (2012) 50–65.
[88] A. Kosari, M. Ahmadi, F. Tichelaar, P. Visser, Y. Gonzalez-Garcia, H. Zandbergen, H. Terryn, J.M.C. Mol, Dealloying-driven cerium precipitation on intermetallic particles in aerospace aluminium alloys, J. Electrochem. Soc. 168 (4) (2021) 041505.
[89] A. Kosari, F. Tichelaar, P. Visser, H. Zandbergen, H. Terryn, J.M.C. Mol, Dealloying-driven local corrosion by intermetallic constituent particles and dispersoids in aerospace aluminium alloys, Corros. Sci. 177 (2020) 108947.
[90] L.M. Young, Microstructural dependence of aqueous environment-assisted crack growth and hydrogen uptake in AA7050, University of Virginia, Charlottesville, VA, Ph.D. diss., 1999.
[91] L. M. Young, R. P. Gangloff, "S-Phase effect on environmental cracking in AA7050," in advances in the metallurgy of aluminum alloys, ed. M. Tiryakioglu, Materials Park, OH: ASM International, 2001, pp. 135.
[92] D.K. Xu, N. Birbilis, P.A. Rometsch, Effect of S-phase dissolution on the corrosion and stress corrosion cracking of an as-rolled Al-Zn-Mg-Cu alloy[J], Corros., J. Sci. Eng. 68 (3) (2012). 035001-1-035001-10.
[93] L. Zhou, K.H. Chen, S.Y. Chen, Y.F. Ding, S.M. Fan, Correlation between stress corrosion cracking resistance and grain-boundary precipitates of a new generation high Zn-containing 7056 aluminum alloy by non-isothermal aging and re-aging heat treatment, J. Alloys Compd. 850 (2021) 156717.
[94] N.J.H. Holroyd, G.M. Scamans, Stress corrosion cracking in Al-Zn-Mg-Cu aluminum alloys in saline environments, Metall. Mater. Trans. A 44 (3) (2013) 1230–1253.
[95] H. Su, H. Toda, K. Shimizu, K. Uesugi, A. Takeuchi, Y. Watanabe, Assessment of hydrogen embrittlement via image-based techniques in Al-Zn-Mg-Cu aluminum alloys, Acta Mater. 176 (2019) 96–108.
[96] E. Schwarzenböck, E. Ollivier, A. Garner, A. Cassell, T. Hack, Z. Barrett, C. Engel, T.L. Burnett, N.J.H. Holroyd, J.D. Robson, P.B. Prangnell, Environmental

cracking performance of new generation thick plate 7000–T7x series alloys in humid air, Corros. Sci. 171 (2020) 108701.
[97] M. Safyari, M. Moshtaghi, T. Hojo, E. Akiyamaa, Mechanisms of hydrogen embrittlement in high-strength aluminum alloys containing coherent or incoherent dispersoids, Corros. Sci. 194 (2022) 109895.
[98] S.P. Knight, K. Pohl, N.J.H. Holroyd, N. Birbilis, P.A. Rometsch, B.C. Muddle, R. Goswami, S.P. Lynch, Some effects of alloy composition on stress corrosion cracking in Al-Zn-Mg-Cu alloys, Corros. Sci. 98 (2015) 50–62.
[99] U. De Francisco, N.O. Larrosa, M.J. Peel, Hydrogen environmentally assisted cracking during static loading of AA7075 and AA7449, Mater. Sci. Eng. A 772 (2020) 138662.
[100] S. Wang, B.H. Luo, Z.H. Bai, C. He, S.Z. Tan, G. Jiang, Effect of Zn: Mg ratios on microstructure and stress corrosion cracking of 7005 alloy, Mater. 12 (2) (2019) 285.
[101] W.X. Shu, L.G. Hou, C. Zhang, F. Zhang, J.C. Liu, J.T. Liu, L.Z. Zhuang, J.S. Zhang, Tailored Mg and Cu contents affecting the microstructures and mechanical properties of high-strength Al-Zn-Mg-Cu alloys, Mater. Sci. Eng. A 657 (2016) 269–283.
[102] L. Jiang, C.S. Wang, H.D. Fu, J. Shen, Z.H. Zhang, J.X. Xie, Discovery of aluminum alloys with ultra-strength and high-toughness via a property-oriented design strategy, J. Mater. Sci. Technol. 98 (2022) 33–43.
[103] T. Dursun, C. Soutis, Recent developments in advanced aircraft aluminium alloys, Mater. Des. 56 (2014) 862–871.
[104] AMS 4205F, Aluminum Alloy, Plate (7010-T7451) 6.2Zn-1.8Cu-2.4Mg-0.13Zr Solution Heat Treated, Stress Relieved, and Precipitation Heat Treated, AMS D Nonferrous Alloys Committee, 2021-10-22.
[105] AMS 4204D, Aluminum Alloy, Plate (7010-T7651) 6.2Zn-1.8Cu-2.4Mg-0.13Zr Solution Heat Treated, Stress Relieved, and Precipitation Heat Treated, AMS D Nonferrous Alloys Committee, 2019-12-27.
[106] AMS 4211C, Aluminum Alloy, Plate (7040-T7451) 6.2Zn-1.9Cu-2.1Mg-0.10Zr Solution Heat Treated, Stress Relieved, and Overaged, AMS D Nonferrous Alloys Committee, 2018-04-03.
[107] AMS 4050K, Aluminum Alloy, Plate (7050-T7451) 6.2Zn-2.3Cu-2.2Mg-0.12Zr Solution Heat Treated, Stress Relieved, and Overaged, AMS D Nonferrous Alloys Committee, 2021-04-22.
[108] AMS 4201G, Aluminum Alloy, Plate (7050-T7651) 6.2Zn-2.3Cu-2.2Mg-0.12Zr Solution Heat Treated, Stress Relieved, and Overaged, AMS D Nonferrous Alloys Committee, 2020-08-20.
[109] AMS 4252C, Aluminum Alloy, Plate (7150-T7751) 6.4Zn-2.4Mg-2.2Cu-0.12Zr Solution Heat Treated, Stress Relieved, and Overaged, AMS D Nonferrous Alloys Committee, 2018-06-15.
[110] AMS 4206C, Aluminum Alloy, Plate (7055-T7751) 8.0Zn-2.3Cu-2.0Mg-0.16Zr Solution Heat Treated, Stress Relieved, and Overaged, AMS D Nonferrous Alloys Committee, 2017-10-10.
[111] AMS 4202E, Aluminum Alloy, Plate (7475-T7351) 1.6Cu-2.2Mg-0.22Cr-5.7Zn Solution Heat Treated, Stress Relieved by Stretching, and Precipitation Heat Treated, AMS D Nonferrous Alloys Committee, 2019-02-04.
[112] AMS 4089F, Aluminum Alloy, Plate (7475-T7651) 1.6Cu-2.2Mg-0.22Cr-5.7Zn Solution Heat Treated, Stress Relieved by Stretching, and Precipitation Heat Treated, AMS D Nonferrous Alloys Committee, 2020-06-18.
[113] AMS 4410A, Aluminum Alloy, Plate (7081-T7451) 7.2Zn-1.5Cu-2.0Mg-0.10Zr Solution Heat Treated, Stress Relieved and Overaged, AMS D Nonferrous Alloys Committee, 2019-05-07.
[114] AMS 4411A, Aluminum Alloy, Plate (7081-T7651) 7.2Zn-1.5Cu-2.0Mg-0.10Zr Solution Heat Treated, Stress Relieved and Overaged, AMS D Nonferrous Alloys Committee, 2019-05-07.
[115] AMS 4470C, Aluminum Alloy, Plate (7085-T7451) 7.5Zn-1.6Cu-1.5Mg-0.12Zr Solution Heat Treated, Stress-Relieved, and Overaged, AMS D Nonferrous Alloys Committee, 2018-12-27.
[116] AMS 4329B, Aluminum Alloy, Plate (7085-T7651) 7.5Zn-1.6Cu-1.5Mg-0.12Zr Solution Heat Treated, Stress-Relieved, and Overaged, AMS D Nonferrous Alloys Committee, 2017-10-10.
[117] AMS 4250C, Aluminum Alloy, Plate 8.1Zn-2.3Mg-1.0Cu-Zr (7449-T7651) Solution Heat Treated, Stress Relieved, and Overaged, AMS D Nonferrous Alloys Committee, 2019-01-02.
[118] AMS 4407A, Aluminum Alloy, Plate (7056-T7651) 9.1Zn-1.6Cu-1.9Mg Solution Heat Treated, Stress Relieved, and Overaged, AMS D Nonferrous Alloys Committee, 2018-03-23.
[119] AMS 4367, Aluminum Alloy, Extruded Profiles 8.9Zn-2.2Cu-2.2Mg-0.15Zr (7136-T74511) Solution Heat Treated, Stress Relieved by Stretching, Straightened, and Overaged, AMS D Nonferrous Alloys Committee, 2016-09-01
[120] AMS 4415B, Aluminum Alloy, Extrusions (7136-T76511, -T76510) 8.9Zn-2.2Cu-2.2Mg- 0.15Zr Solution Heat Treated, Stress-Relieved, Straightened, and Overaged, AMS D Nonferrous Alloys Committee, 2021-09-15.
[121] W. H. Hunt Jr, J. T. Staley, D. A. Lukasak, D. B. Reiser, R. K. Wyss, L. M. Angers, Aluminum alloy product having improved combinations of properties, U.S. Pat. 5221377. (1993) Jun. 22.
[122] V. Dangerfield, K. P. Smith, T. Warner, D. Dumont, Al-Zn-Cu-Mg aluminum base alloys and methods of manufacture and use, U.S. Pat. 8277580 B2. (2012) Oct. 2.
[123] D. Chakrabarti, J. Liu, J. Goodman, G. Venema, R. Sawtell, Aluminum alloy having superior strength-toughness combinations in thick gauges, U.S. Pat. 0150498 A1. (2002) Oct. 17.
[124] R. Benedictus, C. J. Keidel, A. L. Heinz, N. Telioui, Al-Zn-Mg-Cu alloy with improved damage tolerance-strength combination properties, U.S. Pat. 10472707 B2. (2019) Nov. 12.
[125] E. Sarrazin, J. Philippe, Process for fabrication of products made of an aluminium alloy with high toughness and high fatigue resistance, U.S. Pat. 11571189 A1, (2007) Oct. 18.
[126] S.L. Wei, Y. Feng, H. Zhang, C.T. Xu, Y. Wu, Influence of aging on microstructure, mechanical properties and stress corrosion cracking of 7136 aluminum alloy, J. Cent. South Univ. 28 (9) (2021) 2687–2700.
[127] I. Gheorghe, D. C. Malejan, R. Mächler, Aluminum-zinc-magnesium-copper alloy extrusion, U.S. Pat. 7214281 B2. (2007) May 8.
[128] . Whelchel, E. Nizery, D. Koschel, J. C. Ehrstom, T. Warner, Al-Zn-Cu-Mg alloys with high strength and method of fabrication, U.S. Pat. 16650285 A1. (2020) Jul. 23.
[129] R. Benedictus, C. J. Keidel, A. L. Heinz, High strength Al-Zn alloy and method for producing such an alloy product, U.S. Pat. 0034794 A1. (2005) Feb. 17.
[130] J. X. Xie, H. D. Fu, Z. H. Zhang, L. Jiang, Al-Zn-Mg-Cu alloy with ultra-high strength and high toughness and method of fabrication, CN202110187099.0. (2021) Jun. 18
[131] J. X. Xie, Z. H. Zhang, H. D. Fu, L. Jiang, Solution-aging heat treatment process of an ultra-high strength and high toughness Al-Zn-Mg-Cu aluminum alloy, CN202110182923.3. (2021) Jun. 22.
[132] P.X. Dong, S.Y. Chen, K.H. Chen, Effects of Cu content on microstructure and properties of super-high-strength Al-9.3Zn-2.4Mg-xCu-Zr alloy, J. Alloys Compd. 788 (2019) 329–337.
[133] T. Warner, S. Christophe, B. Bernard, Al-Zn-Mg-Cu alloys and products with improved ratio of static mechanical characteristics to damage tolerance, U.S. Pat. 20097550110 B2. (2009) Jun. 23.